Target Characterization and Scattering Power Decomposition for Full and Compact Polarimetric SAR Data

Subhadip Dey, *Graduate Student Member, IEEE*, Avik Bhattacharya, *Senior Member, IEEE*, Debanshu Ratha, *Member, IEEE*, Dipankar Mandal, *Graduate Student Member, IEEE*, and Alejandro C. Frery, *Senior Member, IEEE*

***Abstract*— In radar polarimetry, incoherent target decomposition techniques help extract scattering information from polarimetric synthetic aperture radar (SAR) data. This is achieved either by fitting appropriate scattering models or by optimizing the received wave intensity through the diagonalization of the coherency (or covariance) matrix. As such, the received wave information depends on the received antenna configuration. Additionally, a polarimetric descriptor that is independent of the received antenna configuration might provide additional information which is missed by the individual elements of the coherency matrix. This implies that existing target characterization techniques might neglect this information. In this regard, we suitably utilize the 2-D and 3-D Barakat degree of polarization which is independent of the received antenna configuration to obtain distinct polarimetric information for target characterization. In this study, we introduce new roll-invariant scattering-type parameters for both full-polarimetric (FP) and compact-polarimetric (CP) SAR data. These new parameters jointly use the information of the 2-D and 3-D Barakat degree of polarization and the elements of the coherency (or covariance) matrix. We use these new scattering-type parameters, which provide equivalent information as the Cloude α for FP SAR data and the ellipticity parameter χ for CP SAR data, to characterize various targets adequately. Additionally, we appropriately utilize these new scattering-type parameters to obtain unique non-model-based three-component scattering power decomposition techniques. We obtain the even-bounce, and the odd-bounce scattering powers by modulating the total polarized power by a proper geometrical factor derived using the new scattering-type parameters for FP and CP SAR data. The diffused scattering power is obtained as the depolarized fraction of the total power. Moreover, due to the nature of its formulation, the decomposition scattering powers are non-negative and roll-invariant while the total power is conserved. The proposed method is both qualitatively and quantitatively assessed utilizing the L-band ALOS-2 and C-band Radarsat-2 FP and the associated simulated CP SAR data.**

Manuscript received April 22, 2020; revised June 17, 2020; accepted July 13, 2020. The work of Alejandro C. Frery was supported in part by the Conselho Nacional de Desenvolvimento Científico e Tecnológico (CNPq), and in part by Fapeal, Brazil. *(Corresponding author: Avik Bhattacharya.)*

Subhadip Dey, Avik Bhattacharya, Debanshu Ratha, and Dipankar Mandal are with Microwave Remote Sensing Laboratory, Centre of Studies in Resources Engineering, IIT Bombay, Mumbai 400076, India (e-mail: sdey2307@gmail.com; avikb@csre.iitb.ac.in).

Alejandro C. Frery is with the Universidade Federal de Alagoas, Maceió 57072-900, Brazil, and also with the Key Laboratory of Intelligent Perception and Image Understanding of the Ministry of Education, Xidian University, Xi'an 710071, China (e-mail: acfrery@laccan.ufal.br).

Color versions of one or more of the figures in this article are available online at http://ieeexplore.ieee.org.

Digital Object Identifier 10.1109/TGRS.2020.3010840

***Index Terms*— Compact polarimetry, full polarimetry, scattering-type parameter, target characterization, target decomposition.**

I. Introduction

POLARIMETRIC decompositions aim, among other applications, to characterize scattering mechanisms from a target. Broadly categorizing, target decomposition techniques are divided into two distinct categories: coherent and incoherent. Coherent decomposition techniques utilize information from the 2×2 complex scattering matrix $\mathbf{S}$, whereas incoherent decompositions extract information in terms of the second-order statistics from the 3×3 coherency $\mathbf{T}$ or the covariance $\mathbf{C}$ matrices.

Several methods have been developed to decompose the average covariance or coherency matrices. In this regard, either the eigenvalue/eigenvector-based decomposition methods provide a unique solution to the scattering mechanisms [1], [2], or the roll-invariant scattering descriptors derived using the geodesic distance between Kennaugh matrices [3]. The interpretation of the scattering information is achieved by obtaining a set of unique roll-invariant parameters. On the other hand, model-based decomposition methods utilize the physical and geometrical properties of targets to extract scattering information from second-order statistics.

The pioneering work of Freeman and Durden [4] on the three-component scattering power decomposition (F3D) paved the way for model-based decomposition techniques. The scattering powers obtained from their method were based on the assumption of target reflection symmetry, i.e., $\langle S_{\mathrm{HH}} S_{\mathrm{HV}}^{*} \rangle = \langle S_{\mathrm{VV}} S_{\mathrm{VH}}^{*} \rangle = 0$. The Freeman and Durden decomposition model is simple and easy to implement, and has been utilized for several applications as, for instance, unsupervised classification [5], [6].

However, the reflection symmetry assumption is seldom verified for most of the targets in a typical natural scenario. Therefore, the condition of uncorrelated co-polarized and cross-polarized components does not hold, i.e., $\langle S_{\mathrm{HH}} S_{\mathrm{HV}}^{*} \rangle \neq 0$, and $\langle S_{\mathrm{VV}} S_{\mathrm{HV}}^{*} \rangle \neq 0$. In such a condition, the cross-polarized component, $\langle |S_{\mathrm{HV}}|^2 \rangle$, might be predominant.

In this regard, Yamaguchi *et al.* [7] proposed a four-component model-based decomposition, which incorporates a helix as a fourth component.

In both the Freeman-Durden [4] and Yamaguchi [7] decompositions, the primary scatterer from vegetation canopy is modeled as a thin cylinder. However, such a description is often too simplistic for the complex structural configuration of most vegetation canopies.

Hence, Arii *et al.* [8] proposed an nth power of cosine squared function to describe such complex canopy structures. Nonetheless, this study considered the canopy scattering as the dominant mechanism. Similarly, Neumann *et al.* [9] proposed the retrieval of forest parameters using polarimetric interferometric synthetic aperture radar (SAR) data. This study combined the physical model-based decomposition with a random volume over the ground inversion approach.

Van Zyl *et al.* [10] proposed constraints to grant nonnegative eigenvalues. Similarly, Cui *et al.* [11] performed the complete decomposition of the coherency matrix into one volume component and two single-scattering components using a nonnegative power constraint. Hence, this decomposition technique was able to overcome the negative power problem.

The aforementioned model-based decompositions did not take into account the target orientation aspect with the radar line of sight. Within a radar resolution cell, targets can be randomly oriented about the radar line of sight and, thus, can have diverse polarimetric responses. Several studies attempted to compensate this target orientation effect [12]–[15]. The central idea behind orientation compensation techniques is to reduce the contribution of the cross-polarized component. In other words, these techniques minimize the overestimation of the volume scattering power while increasing the even-bounce scattering power. Later, Bhattacharya *et al.* [16] utilized the degree of polarization of the scattered wave as an adaptive parameter to improve the scattering power components of the Yamaguchi four-component decomposition. Chen *et al.* [17] proposed a generalized double and odd-bounce scattering models by separating them with their independent orientation angles.

An alternative approach to determine the orientation of a target while improving the scattering powers is statistical information theory. In this regard, Bhattacharya *et al.* [18] optimized the Hellinger distance between orthogonal and rotated urban targets to the radar line of sight to determine the orientation angle and, finally, modifying the Yamaguchi four-component decomposition powers. Later, Eltoft and Doulgeris [19] extended the model-based decomposition techniques by introducing higher order distribution functions and radar texture models. An and Lin [20] reconsidered the problem of negative scattering powers and the overestimation of the volume scattering component in the Freeman-Durden decomposition. They proposed a methodology to completely decompose an arbitrary coherency matrix into several polarimetric symmetry components.

Stability of decomposition powers poses a significant challenge in several model-based decompositions. Jiao *et al.* [21] proposed a stable three-component decomposition by solving a constraint optimization problem. Shuang *et al.* [22] combined a new condition with the Freeman-Durden decomposition to distinguish human-made structure and nature media after orientation angle compensation.

Chen *et al.* [23] provided a review of decomposition techniques using polarimetric SAR data.

Full polarimetric (FP) SAR data provides optimum performance in target characterization due to its complete radar target information content. However, compact polarimetric (CP) SAR data offers more information than a single or dual-polarized SAR data, while covering larger swath widths when compared with FP SAR systems.

In CP radars, the relative phase between the two received polarizations is retained, unlike the conventional dual-polarized SAR systems. In the $\pi/4$ mode [24], the transmitted polarization is a superposition of the linear horizontal (H) and vertical polarization (V) oriented at 45° to the horizontal. The dual-circular compact polarimetry (DCP) model proposed in [25] used right circular polarization on transmit, and right and left circular polarization on receive. Furthermore, Raney [26] proposed a new hybrid-polarity architecture, consisting of circular transmit and orthogonal linear polarizations receive. This new hybrid-pol architecture preserves all the information of the DCP mode since the Stokes parameter of electromagnetic (EM) wave does not depend on the received polarization basis [27].

Raney [26] and Raney *et al.* [28] proposed the m-δ and m-χ decomposition methods for the hybrid-CP SAR data, respectively, where m indicates the degree of polarization of the scattered EM wave. The performance of the m-δ decomposition largely depends on the purity in the transmission polarization of the EM wave. Hence, the phase difference parameter, δ, provides better results only when the transmitted wave is perfectly circular. On the contrary, the ellipticity, χ, is robust toward the transmitting wave polarization. While characterizing the scattering phenomenon from the lunar surface, Raney *et al.* [28] pointed out the ability of the m-χ decomposition to resolve certain even-odd bounce scattering ambiguity over lunar crater walls. Later, the authors hypothesized that a three-component (m-χ-ψ) decomposition would be more appropriate to discriminate different scattering mechanisms with *a priori* information of the transmitting ellipticity (χ) of the EM wave. This striking idea was exploited by Bhattacharya *et al.* [29] while proposing the S-Ω decomposition, where Ω depends on m, the transmitting wave ellipticity (χ_t), and orientation (ψ_t), and the received wave ellipticity (χ_r) and orientation (ψ_r).

Incoherent target decomposition techniques might not utilize CP information present in SAR data. In particular, such techniques for FP SAR data optimize the received wave intensity through the diagonalization of the coherency (or covariance) matrix [2], [30], [31]. Hence, the information provided by a parameter which is received antenna basis invariant might be useful. In this respect, the degree of polarization obtained from the n dimensional (nD) coherency matrix proposed by Barakat [32], [33] can be suitably utilized to gain enhanced polarimetric information. The Barakat degree of polarization is linked to the polarimetric contribution of the Shannon entropy [34].

In this study, we jointly use the 3-D and 2-D Barakat degree of polarization [33], and the elements of the coherency (or covariance) matrix to obtain roll-invariant scattering-type

parameters for both FP and CP monostatic SAR data. These parameters are equivalent to the Cloude and Pottier parameter α [1] for FP SAR data, and the wave ellipticity parameter χ for CP SAR data. Additionally, we propose novel three-component scattering power decomposition techniques for both FP and CP SAR data by utilizing the scattering-type parameter and the 3-D and 2-D Barakat degree of polarization.

Unlike traditional model-based decompositions, the proposed methods do not utilize any particular scattering models for the estimation of the scattering powers, and the formulations of these two techniques are equivalent for both FP and CP SAR data. Moreover, each power component is guaranteed to be nonnegative, and the total power is conserved. The proposed "nonmodel" based three-component scattering power decomposition techniques are applied to full and simulated hybrid-CP L-band ALOS-2 and C-band RS-2 SAR data over Mumbai and San Francisco (SF), respectively. The effectiveness of the proposed methods is used for qualitative analysis of scattering mechanisms and quantitative analysis of the scattering powers.

This work unfolds as follows. We derive the new target scattering-type parameters for FP and CP SAR data in Section II; those parameters are further utilized to obtain unique three-component nonmodel-based scattering power decompositions for two data sets. In Section III, we compare the results obtained from the proposed techniques with other existing target characterization parameters and decomposition techniques. Sections III-A1 and III-B1 compare the proposed target characterization parameters with the ones existing in literature for FP and CP data. Accordingly, Sections III-A2 and III-B2 present and compare the proposed 3-component nonmodel-based decomposed powers with two decomposition techniques for FP and CP SAR data, respectively. Finally, Section IV summarizes the proposed methodologies and concludes by highlighting its advantages and limitations for different SAR data.

II. Methodology

We introduce new roll-invariant scattering-type parameters by utilizing the 3-D and 2-D Barakat degree of polarization [33] (m) and the elements of the 3×3 coherency and the 2×2 covariance matrix for both FP and CP SAR data, respectively. In this regard, we use the expression derived from [33] to calculate the 3-D and 2-D Barakat degree of polarization. Subsequently, we use these scattering-type parameters to obtain nonmodel based three-component scattering power decompositions for both FP and CP SAR data. We obtain the even-bounce and the odd-bounce powers by modulating the total polarized power by a specific geometrical factor easily derived using the new scattering-type parameters for both FP and CP SAR data.

A. Full Polarimetry

In FP SAR, the 2×2 complex scattering matrix $\mathbf{S}$ encompasses complete polarimetric information about backscattering from targets for each pixel. It is expressed in the backscatter alignment (BSA) convention in the linear horizontal (H) and linear vertical (V) polarization basis as

$$\mathbf{S} = \begin{bmatrix} S_{\mathrm{HH}} & S_{\mathrm{HV}} \\ S_{\mathrm{VH}} & S_{\mathrm{VV}} \end{bmatrix} \;\Rightarrow\; \boldsymbol{k} = V([\mathbf{S}]) = \frac{1}{2}\mathrm{Tr}(\mathbf{S}\Psi) \tag{1}$$

where $V(\cdot)$ is the vectorization operator on the scattering matrix, Ψ is the corresponding basis matrix, and Tr is the sum of the diagonal elements of the matrix. Each element of the matrix represents the backscattering response of the target at a specific polarization. The diagonal elements of the matrix represent the copolarized scattering information, while the off-diagonal terms represent the cross-polarized information. In the monostatic backscattering case, the reciprocity theorem constrains the scattering matrix to be symmetric, i.e., $S_{\mathrm{HV}} = S_{\mathrm{VH}}$.

The multilooked Hermitian positive semi-definite 3×3 coherency matrix $\mathbf{T}$ is obtained from the averaged outer product of the target vector $\boldsymbol{k}_P$ (derived using the Pauli basis matrix, Ψ_P) with its conjugate. Similarly, the 3×3 covariance matrix $\mathbf{C}$ is obtained from the averaged outer product of the target vector $\boldsymbol{k}_L$ (derived using the Lexicographic basis matrix, Ψ_L) with its conjugate

$$\Psi_P = \left\{ \sqrt{2}\begin{bmatrix} 1 & 0 \\ 0 & 1 \end{bmatrix}, \sqrt{2}\begin{bmatrix} 1 & 0 \\ 0 & -1 \end{bmatrix}, \sqrt{2}\begin{bmatrix} 0 & 1 \\ 1 & 0 \end{bmatrix} \right\}$$
$$\Psi_L = \left\{ 2\begin{bmatrix} 1 & 0 \\ 0 & 0 \end{bmatrix}, 2\sqrt{2}\begin{bmatrix} 0 & 1 \\ 0 & 0 \end{bmatrix}, 2\begin{bmatrix} 0 & 0 \\ 0 & 1 \end{bmatrix} \right\}.$$

Similar to the conventional degree of polarization, the 3-D Barakat degree of polarization ($0 \leq m \leq 1$) also characterizes the state of polarization (or purity) of an EM wave. For a completely polarized EM wave, $m = 1$ and for a completely unpolarized EM wave, $m = 0$. In between these two extreme cases, the EM wave is said to be partially polarized, $0 < m < 1$.

Barakat [32] provided an expression of m for the $n \times n$ coherency matrix. This expression is used in this study to obtain the 3-D Barakat degree of polarization m_{FP} from the 3×3 coherency matrix $\mathbf{T}$ for FP SAR data as

$$m_{\mathrm{FP}} = \sqrt{1 - \frac{27|\mathbf{T}|}{(\mathrm{Tr}(\mathbf{T}))^3}} \tag{2}$$

where $|\cdot|$ is the determinant of a matrix. It should be noted that although this quantity is related to the conventional degree of polarization, it is not the overall degree of polarization for the FP case as it does not include all the invariants. The coherency (or covariance) matrix can be used to estimate this quantity considering suitable ergodicity properties.

Let us assume that

$$\tan\eta_1 = \frac{T_{11}}{m_{\mathrm{FP}}\,\mathrm{Span}} \quad \text{and} \quad \tan\eta_2 = \frac{T_{22}+T_{33}}{m_{\mathrm{FP}}\,\mathrm{Span}} \tag{3}$$

where T_{11}, T_{22}, and T_{33} are the diagonal elements of the coherency matrix, and denote

$$\mathrm{Span} = T_{11} + T_{22} + T_{33}. \tag{4}$$

Therefore, using a simple relationship, we obtain

$$\begin{aligned} \tan\theta_{\mathrm{FP}} &= \tan(\eta_1 - \eta_2) \\ &= \frac{m_{\mathrm{FP}}\,\mathrm{Span}\,(T_{11} - T_{22} - T_{33})}{T_{11}(T_{22}+T_{33}) + m_{\mathrm{FP}}^2\,\mathrm{Span}^2}. \end{aligned} \tag{5}$$

Appendixes A1 and B prove that $\theta_{\rm FP} \in [-45°, 45°]$ is a roll-invariant parameter. This parameter can be used to characterize scattering-type information from targets.

It can be observed from (5), that when $m_{\rm FP} = 0$ (i.e., when no polarization structure exists in the scattered EM wave), then $\theta_{\rm FP} = 0$. Whereas, when $m_{\rm FP} = 1$, then either $\theta_{\rm FP} = -45°$ or $\theta_{\rm FP} = 45°$, depending on the scattering from a dihedral or a trihedral target, respectively. Otherwise, for all other cases, $\theta_{\rm FP} \in (-45°, 45°)$.

We split the total power (Span) into two components: even-bounce ($P_d^{\rm FP}$) and odd-bounce ($P_s^{\rm FP}$) scattering powers using a geometrical factor ($1 \pm \sin 2\theta_{\rm FP}$) using the 3-D Barakat degree of polarization $m_{\rm FP}$ (2) and the scattering-type information $\theta_{\rm FP}$ (5). The diffused scattering power ($P_v^{\rm FP}$) is obtained as the depolarized fraction of the total power

$$P_d^{\rm FP} = \frac{m_{\rm FP}\,{\rm Span}}{2}(1 - \sin 2\theta_{\rm FP}) \tag{6}$$

$$P_v^{\rm FP} = {\rm Span}\,(1 - m_{\rm FP}), \quad \text{and} \tag{7}$$

$$P_s^{\rm FP} = \frac{m_{\rm FP}\,{\rm Span}}{2}(1 + \sin 2\theta_{\rm FP}). \tag{8}$$

When $m_{\rm FP} = 0$, then $P_d^{\rm FP} = P_s^{\rm FP} = 0$, and $P_v^{\rm FP} = {\rm Span}$. This corresponds to the complete depolarized case. For pure even-bounce scattering, $m_{\rm FP} = 1$ and $\theta_{\rm FP} = -45°$ with $P_s^{\rm FP} = P_v^{\rm FP} = 0$, and $P_d^{\rm FP} = {\rm Span}$. For pure odd-bounce scattering, $m_{\rm FP} = 1$ and $\theta_{\rm FP} = 45°$ with $P_d^{\rm FP} = P_v^{\rm FP} = 0$, and $P_s^{\rm FP} = {\rm Span}$. It is noteworthy that the scattering power components are nonnegative, and that the total power (Span) is conserved for any polarization state.

B. Compact Polarimetry

The hybrid CP mode measures a projection of the 2×2 complex scattering matrix $\mathbf{S}$ as

$$\begin{bmatrix} E_{\rm CH} \\ E_{\rm CV} \end{bmatrix} = \frac{1}{\sqrt{2}} \begin{bmatrix} S_{\rm HH} & S_{\rm HV} \\ S_{\rm VH} & S_{\rm VV} \end{bmatrix} \begin{bmatrix} 1 \\ \pm i \end{bmatrix} = \frac{1}{\sqrt{2}} \begin{bmatrix} S_{\rm HH} \pm i\,S_{\rm HV} \\ S_{\rm VH} \pm i\,S_{\rm VV} \end{bmatrix} \tag{9}$$

where the subscript C can be either the left-hand circular (LHC) transmit with a $+$ sign or the right-hand circular (RHC) transmit with a $-$ sign. The 2×2 covariance matrix $\mathbf{C}_2$ is then obtained from the elements of the scattering vector as

$$\mathbf{C}_2 = \begin{bmatrix} \langle |E_{\rm CH}|^2 \rangle & \langle E_{\rm CH} E_{\rm CV}^* \rangle \\ \langle E_{\rm CV} E_{\rm CH}^* \rangle & \langle |E_{\rm CV}|^2 \rangle \end{bmatrix}. \tag{10}$$

For CP-SAR data, the 4×1 Stokes vector $\vec{\mathbf{S}}$ can be written in terms of the elements of the 2×2 covariance matrix $\mathbf{C}_2$

$$\vec{\mathbf{S}} = \begin{bmatrix} S_0 \\ S_1 \\ S_2 \\ S_3 \end{bmatrix} = \begin{bmatrix} C_{11} + C_{22} \\ C_{11} - C_{22} \\ C_{12} + C_{21} \\ \pm j\,(C_{12} - C_{21}) \end{bmatrix} \tag{11}$$

where $\pm$ corresponds to the left and right circular polarizations, respectively.

The first element of the Stokes vector, S_0, is a measure of the total average received power. The third element, S_3, is a measure of the average received power in circular polarization. The handedness of this circular polarization can be inferred from the sign ($\pm$) of the S_3 component.

The proportion of the power that is received by the radar in opposite-sense circular (OC) polarization to that transmitted is $(S_0 + S_3)/2$. For example, ${\rm OC} = (S_0 + S_3)/2 = |E_{\rm R}|^2$ for left-circular (L) polarization on transmit, where $|E_{\rm R}|^2$ is the intensity of the right-circular component. Such a change of polarity occurs when an EM wave undergoes an odd number of reflections.

Similarly, $(S_0 - S_3)/2$ is a measure of the power received by the radar in the same-sense circular (SC) polarization as it was transmitted, which represents an even number of reflections. For example, ${\rm SC} = (S_0 - S_3)/2 = |E_{\rm L}|^2$ for left-circular (L) polarization on transmit, where $|E_{\rm L}|^2$ is the intensity of the left-circular component.

Similar to the FP case, we use the Barakat formulation to obtain the 2-D Barakat degree of polarization $m_{\rm CP}$ from the 2×2 covariance matrix $\mathbf{C}_2$ for CP SAR data as

$$m_{\rm CP} = \sqrt{1 - \frac{4|\mathbf{C}_2|}{({\rm Tr}(\mathbf{C}_2))^2}}. \tag{12}$$

Similar to the FP case, let us assume

$$\tan\zeta_1 = \frac{\rm OC}{m_{\rm CP}\,S_0} \quad \text{and} \quad \tan\zeta_2 = \frac{\rm SC}{m_{\rm CP}\,S_0} \tag{13}$$

with,

$$S_0 = {\rm SC} + {\rm OC}. \tag{14}$$

Therefore, using a simple relationship, we obtain

$$\tan\theta_{\rm CP} = \tan(\zeta_1 - \zeta_2) = \frac{m_{\rm CP}\,S_0\,({\rm OC} - {\rm SC})}{{\rm OC} \times {\rm SC} + m_{\rm CP}^2\,S_0^2}. \tag{15}$$

It can be observed from Appendix A2 that $\theta_{\rm CP} \in [-45°, 45°]$ characterizes scattering-type information from targets utilizing the SC and OC polarization scattered powers.

From (15), when $m_{\rm CP} = 0$, i.e. when no polarization structure exists in the EM wave, then $\theta_{\rm CP} = 0$. Whereas, when $m_{\rm CP} = 1$, then either $\theta_{\rm CP} = -45°$ or $\theta_{\rm CP} = 45°$, depending on the sense (i.e., right or left circular) of the received polarization with respect to the transmit polarization. Otherwise, for all other cases, $\theta_{\rm CP} \in (-45°, 45°)$.

Analogously to the FP case, the 2-D Barakat degree of polarization $m_{\rm CP}$, and the scattering-type information $\theta_{\rm CP}$, can be used to split the total average received power (S_0) into two components: even-bounce ($P_d^{\rm CP}$), and odd-bounce ($P_s^{\rm CP}$) using a geometrical factor ($1 \pm \sin 2\theta_{\rm CP}$). Similarly, the diffused scattering power ($P_v^{\rm CP}$) is the depolarized fraction of the total power:

$$P_d^{\rm CP} = \frac{m_{\rm CP}\,S_0}{2}(1 - \sin 2\theta_{\rm CP}), \text{ and} \tag{16}$$

$$P_v^{\rm CP} = S_0\,(1 - m_{\rm CP}) \tag{17}$$

$$P_s^{\rm CP} = \frac{m_{\rm CP}\,S_0}{2}(1 + \sin 2\theta_{\rm CP}). \tag{18}$$

In the case of scattering power decomposition, when $m_{\rm CP} = 0$, $P_d^{\rm CP} = P_s^{\rm CP} = 0$, and $P_v^{\rm CP} = S_0$. This corresponds to the complete depolarized case. For pure even-bounce scattering,

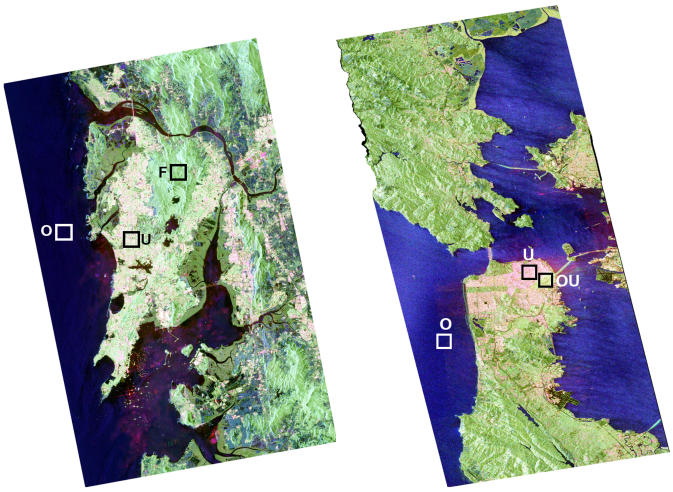

(a) (b)

Fig. 1. Pauli RGB images of (Left) ALOS-2 L-band acquisition over Mumbai, India and (Right) RS-2 C-band acquisition over SF, USA. (a) Pauli RGB, Mumbai. (b) Pauli RGB, SF.

$m_{\rm CP} = 1$ and $\theta_{\rm CP} = -45°$ with $P_s^{\rm CP} = P_v^{\rm CP} = 0$, and $P_d^{\rm CP} = S_0$. For pure odd-bounce scattering, $m_{\rm CP} = 1$ and $\theta_{\rm CP} = 45°$ with $P_d^{\rm CP} = P_v^{\rm CP} = 0$, and $P_s^{\rm CP} = S_0$. Moreover, the total power (S_0) is conserved for any polarization state.

III. Results

In Section II, we derived two roll-invariant scattering-type parameters, $\theta_{\rm FP}$ and $\theta_{\rm CP}$ by jointly utilizing the 3-D and 2-D Barakat degree of polarization and the elements of the coherency and covariance matrices for FP and CP imaging modes respectively. Nevertheless, their physical interpretation is comparable to some of the established parameters known in the literature, viz., Cloude and Pottier's α [1] for FP SAR data, and Raney *et al.*'s χ [28] for CP SAR data. This section provides a comparison of $\theta_{\rm FP}$ and $\theta_{\rm CP}$ with $\overline{\alpha} = 45° - \alpha$ and $\overline{\chi} = -\chi$ respectively. The translations of α and χ to $\overline{\alpha}$ and $\overline{\chi}$, respectively, are presented solely to compare the scattering nature of the targets in the same range. We have also briefly analyzed the polarimetric scattering entropy, H for the two imaging modes over some regions of interest.

We used two FP SAR images over Mumbai, India, and SF, USA, shown in Fig. 1. The Mumbai scene is an L-band ALOS-2 image with a center incidence angle of 33°. The image is multilooked by a factor of 3 in range direction, and 5 in the azimuth direction to generate 15 m^2 pixels.

The SF scene is a C-band RS-2 image acquired with near and far range incidence angles of 28.02° and 29.81°, respectively. The single look complex (SLC) image is multilooked by a factor of 2 in the range direction, and 4 in the azimuth direction to generate a 20 m^2 ground pixel.

Additionally, we generated simulated hybrid-CP data from both the FP SAR data sets with an ellipticity angle of −45° (right circular) and 0° orientation angle.

A. Full Polarimetry

Figs. 2 and 3 show the images of $\theta_{\rm FP}$ and $\overline{\alpha}$ for the ALOS-2 L-band and RS-2 C-band SAR data, respectively. It can be seen that $\theta_{\rm FP}$ provides better contrast over different land cover classes with two different frequencies than $\overline{\alpha}$.

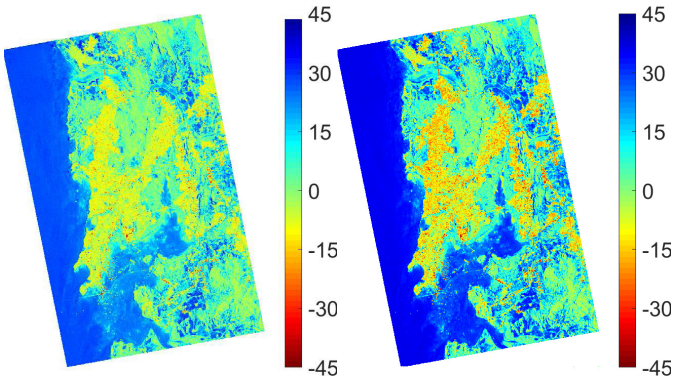

(a) (b)

Fig. 2. Images of $\overline{\alpha}$ and $\theta_{\rm FP}$ for ALOS-2 FP SAR data over Mumbai. (a) $\overline{\alpha}$. (b) $\theta_{\rm FP}$.

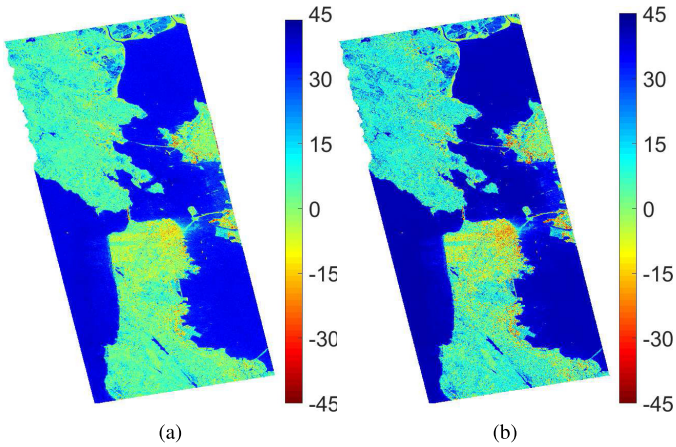

(a) (b)

Fig. 3. Images of $\overline{\alpha}$ and $\theta_{\rm FP}$ for RS-2 FP SAR data over SF. (a) $\overline{\alpha}$. (b) $\theta_{\rm FP}$.

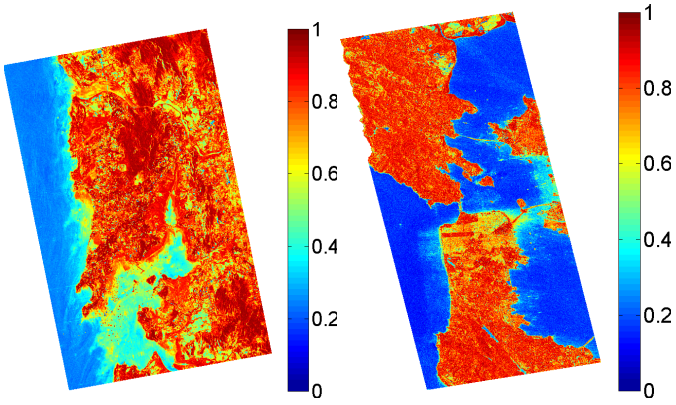

(a) (b)

Fig. 4. Images of H for (a) ALOS-2 FP and (b) RS-2 FP SAR data over Mumbai and SF, respectively.

Figs. 5 and 6 show histograms of $\overline{\alpha}$, $\theta_{\rm FP}$ and $m_{\rm FP}$, along with their notched boxplots (the notches are approximate confidence intervals for the median at 95%), over selected areas of FP images, identified as "U," "O," and "F" / "OU" in Fig. 1. In the ALOS-2 FP data, "U" denotes the urban area, "O" denotes the ocean area, and "F" denotes the forest area; while in the RS-2 FP data, "U" denotes urban area, "O" denotes ocean area and "OU" denotes the oriented urban area.

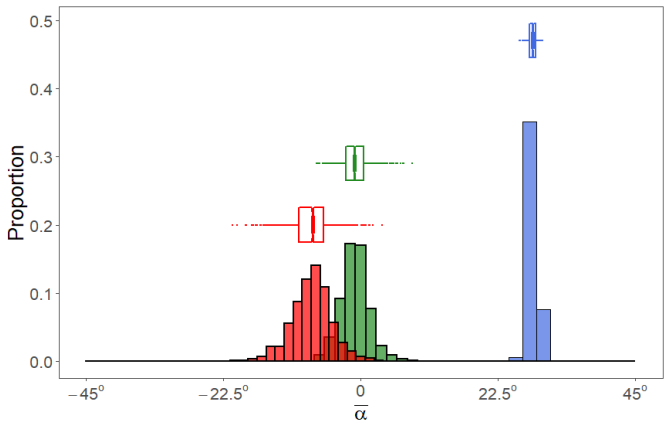

(a)

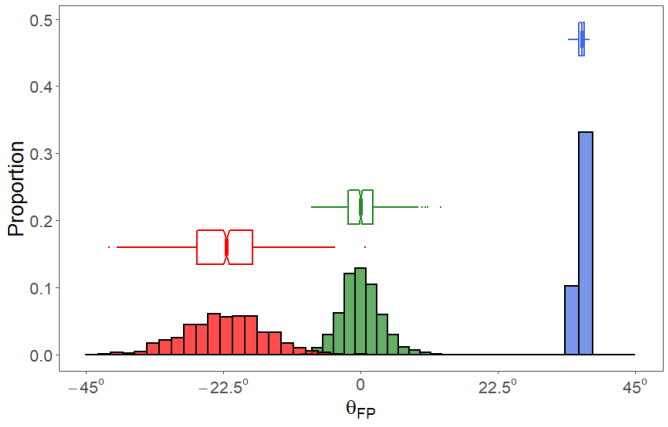

(b)

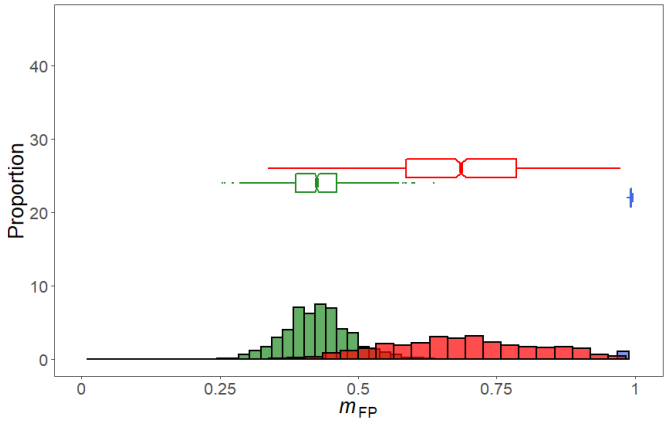

(c)

Fig. 5. Comparison of θ_{FP} with $\overline{\alpha}$ and m_{FP} for "U" (red), "F" (green) and "O" (blue) over FP ALOS-2 L-band data. (a) $\overline{\alpha}$. (b) θ_{FP}. (c) m_{FP}.

1) Comparison of θ_{FP} With $\overline{\alpha}$: Figs. 5 and 6 show that both $\overline{\alpha}$ and θ_{FP} follow a similar trend over the land-cover types which indicates comparable behavior for characterizing scattering-types from different targets.

Over the region "O," the ocean area of ALOS-2 FP data, (Fig. 5), the 3-D Barakat degree of polarization (m_{FP}) varies between 0.95 and 1, and both θ_{FP} and $\overline{\alpha}$ are +ve valued. Besides this, we can observe in Fig. 4 that the values of H over this region is also low (0.1–0.3). In general, when the ocean surface is smooth, co-polarized backscatter signatures show a low coefficient of variation, which is associated with a high 3-D Barakat degree of polarization [35]. Alongside this, over the ocean surface, an odd-bounce scattering mechanism dominates due to which both θ_{FP} and $\overline{\alpha}$ show high +ve values. However, the value of $\overline{\alpha}$ is roughly between 27° and 29°, whereas the value of θ_{FP} is around 35°–37°. This indicates that θ_{FP} is able to better characterize purer odd-bounce scattering mechanism than $\overline{\alpha}$.

Similar to m_{FP} over "O," the value of m_{FP} over "U" is also high. However, the values of $\overline{\alpha}$ and θ_{FP} lead to infer the presence of even-bounce scattering from these urban areas. Besides, the value of θ_{FP} is around 8°–12° higher than $\overline{\alpha}$. In contrast, the value of m_{FP} over "F" is low, which might be due to multiple scattering of the EM wave with distributed targets over moderately dense vegetated areas [36]. The value of m_{FP} is around 0.3–0.6 over the vegetation area, which suggests a certain amount of polarization structure in the wave. This can be attributed to small fluctuations of θ_{FP} in the range −8.0°–12.0° over this region as seen in Fig. 5.

Fig. 6 shows a comparison between $\overline{\alpha}$ and θ_{FP} for the C-band RS-2 image over SF and Fig. 4(b) shows the spatial distribution of H over the same region. The behavior of the data suggests a higher discriminating power of θ_{FP} over $\overline{\alpha}$. Similar to the ALOS2 FP data, Fig. 6 shows the high values of m_{FP} over "O" in ocean surface. It is known that odd-bounce scattering dominates over the ocean surface; this is confirmed by values of $\theta_{FP} \approx 42°$, which are higher than $\overline{\alpha} \approx 38°$. Hence, θ_{FP} indicates a purer scattering-type than $\overline{\alpha}$.

The "OU" region is an urban area that is oriented obliquely about the radar line of sight. This orientation contributes a strong cross-polarization component [37], [38] which decreases the value of m_{FP} and increases the values of H over this region as shown in Fig. 4. However, the values of θ_{FP} indicate the presence of even-bounce scatterers better than $\overline{\alpha}$ by $\approx 6°$. Over the orthogonal urban area, "U," the range of θ_{FP} is $\approx -18°$ to $-23°$, while the range of $\overline{\alpha}$ is $\approx -5°$ to $-12°$. Over this area, m_{FP} ranges between 0.78 and 0.82. Also, the substantial contributions of odd-bounce scattering component in this area influenced the ranges of both θ_{FP} and $\overline{\alpha}$.

Hence, it is noteworthy that, for both the L- and C-band SAR images, θ_{FP} can extract more information from the scattered wave component and, thus, it is more useful for enhanced target characterization than $\overline{\alpha}$. This improved ability is likely to be due to the joint utilization of 3-D Barakat degree of polarization and received wave information in θ_{FP}.

2) Decomposed Power Components: We use the proposed target scattering-type parameter θ_{FP} to develop a new three-component scattering power decomposition technique, as given in (6)–(8). We compare the even-bounce (P_d^{FP}), diffused (P_v^{FP}), and odd-bounce (P_s^{FP}) scattering power components for the proposed technique and the even-bounce, odd-bounce, and volume scattering powers for the Freeman-Durden three-component scattering power decomposition (F3D) and the Yamaguchi four-component model-based decomposition (Y4R), obtained with the L-band ALOS-2 Mumbai images for different scattering targets.

The dominant odd-bounce scattering power is apparent from the three decompositions over the ocean surface ("O") while

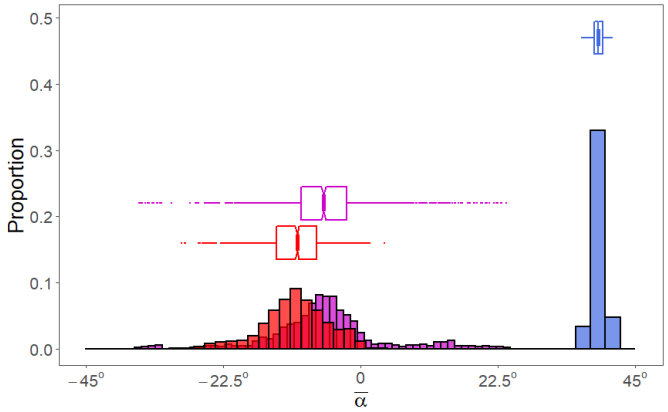

(a)

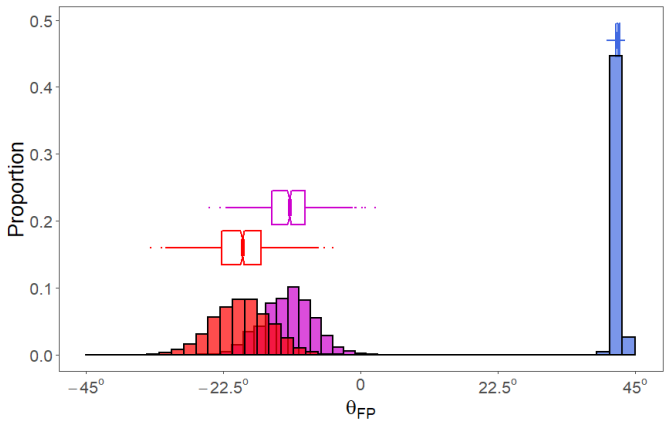

(b)

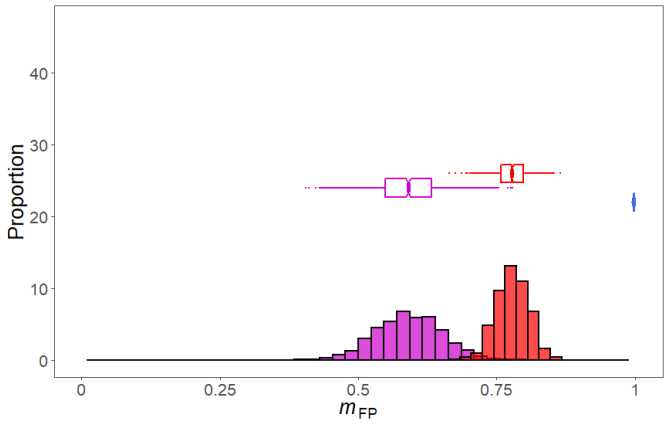

(c)

Fig. 6. Comparison of θ_{FP} with $\overline{\alpha}$ and m_{FP} for "U" (red), "OU" (magenta), and "O" (blue) over FP RS-2 C-band data. (a) $\overline{\alpha}$. (b) θ_{FP}. (c) m_{FP}.

the entropy is also low ($H \approx 0.1$–0.3) as compared to other scattering targets as seen in Fig. 4. Here, the sample mean values of P_s^{FP} are -11.35 dB and -11.36 dB for F3D and Y4R, respectively, whereas the mean value is -11.11 dB for the proposed decomposition. This shows an increase of the odd-bounce scattering power by 2%–3% which is mainly due to the ability of the proposed technique to extract appropriate power component from pure targets.

In general, an ocean surface is moderately smooth. Hence, the fraction of the diffused scattering component should be minimal in the total scattering power. In this regard, the sample mean value of P_v^{FP} obtained from the proposed method is -32.36 dB, whereas the sample mean value for the volume scattering power for both F3D and Y4R is ≈ -20.73 dB. Therefore, the proposed technique provides a significant and desired decrease (≈ 11.63 dB) in the value of the diffused scattering component.

On the one hand, over the urban area ("U"), the sample mean value of P_d^{FP} obtained from the proposed decomposition technique is 0.27 and 0.52 dB higher than the P_d^{FP} obtained from Y4R and F3D, respectively. On the other hand, the value of the diffused scattering component, P_v^{FP} over the forest area ("F"), is 0.4 and 0.6 dB lower than the volume scattering powers for Y4R and F3D, respectively. Moreover, Fig. 7 shows an increase in the even-bounce scattering power over the forest area ("F"). An and Lin [20] reported a similar result from a forest area. Thus, the inclusion of the 3-D Barakat degree of polarization is useful to obtain the desired results from diverse targets.

Fig. 7 shows the results of applying the three decomposition techniques to the ALOS-2 image over Mumbai. Fig. 7(a)–(c) shows, respectively, the images produced by F3D, Y4R, and the proposed decomposition technique. Fig. 7 shows the percentage of the power components over urban, ocean, and forest areas, respectively, to provide a qualitative analysis of these results.

Over the urban area the proposed technique shows an even-bounce scattering power of 83.5% while the even-bounce scattering power is 78.6% for F3D and 79.1% for Y4R. In contrast, the diffused power component is 1.1% for the proposed technique, while the volume scattering powers are 7.6% and 2.9% for F3D and Y4R, respectively. These results are illustrated in Fig. 7(d)–(f).

The proposed technique increases the odd-bounce scattering power over the ocean by 13.4% with respect to F3D, and by 7.9% with respect to Y4R. Fig. 7(g)–(i) illustrate these results.

On the other hand, over the forest area, "F," the proposed technique decreases the diffused scattering power by 7.3% with respect to the volume scattering power for F3D, and by 3% with respect to Y4R, which are evident from Fig. 7(j)–(l), respectively.

In general, these differences between the diffused and the volume scattering powers might be due to the utilization of different volume scattering models in model-based decomposition techniques. Besides, an increase in even-bounce power is also evident in the plot. This might be because of the ability of the L-band wave to penetrate the vegetation canopy and interact with the ground and trunks. It may be noted that An and Lin [20] also addressed a similar increase in even-bounce power.

Fig. 8 shows the comparison of the even-bounce (P_d^{FP}), diffused (P_v^{FP}), and odd-bounce (P_s^{FP}) scattering power components for the proposed technique and the powers from F3D and Y4R for the C-band RS-2 SF image.

Over the ocean surface ("O"), the value of H is low and the dominant odd-bounce scattering power is apparent from the three decompositions. Here, the proposed technique shows increased odd-bounce power by ≈ 0.16 and ≈ 0.18 dB as

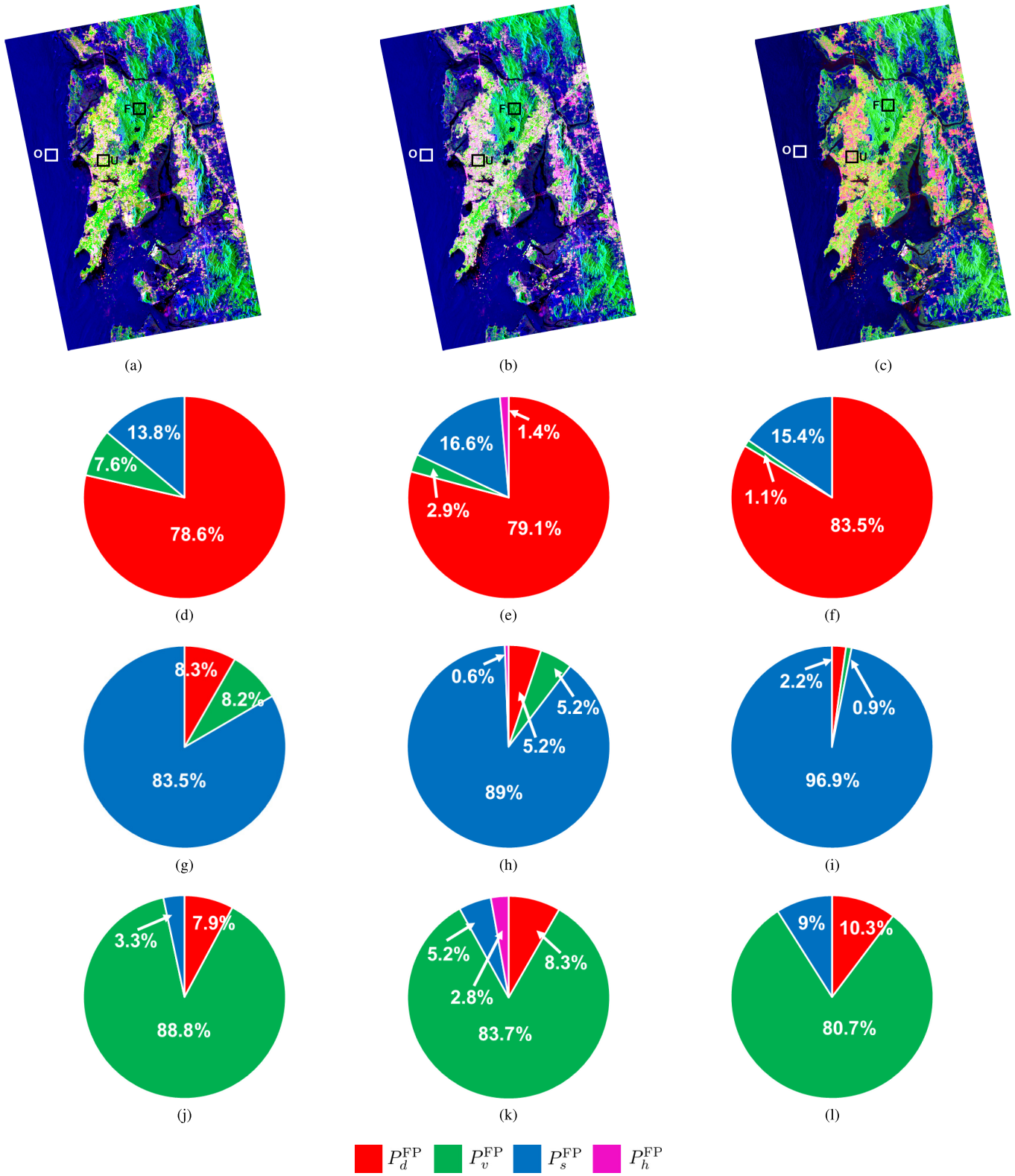

Fig. 7. Comparison of the proposed full-pol decomposition powers with Freeman (F3D) and Yamaguchi four-component decomposition with rotation (Y4R) powers over different areas for FP L-band ALOS-2 SAR data over Mumbai, India. (a) F3D. (b) Y4R. (c) Proposed. (d) F3D: U. (e) Y4R: U. (f) Proposed: U. (g) F3D: O. (h) Y4R: O. (i) Proposed: O. (j) F3D: F. (k) Y4R: F. (l) Proposed: F.

compared to the Y4R and F3D decompositions, respectively. The increase in the even-bounce scattering power over the rotated urban area ("OU") is noteworthy. The even-bounce scattering power for the proposed technique is ≈1.65 dB higher than F3D, and ≈1.15 dB higher than Y4R. Even though m_{FP} varies between 0.3 and 0.6 over the rotated urban area,

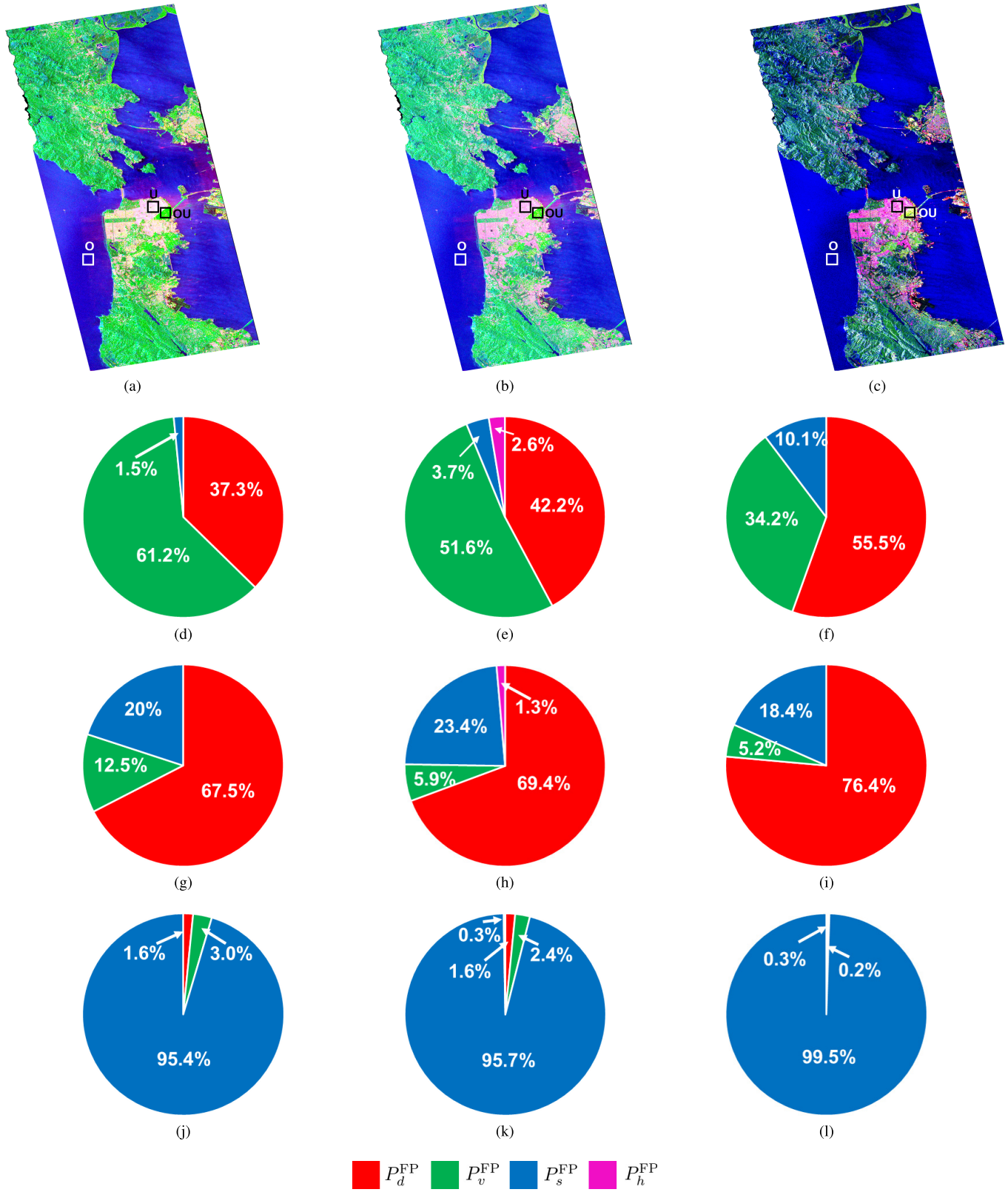

Fig. 8. Comparison of the proposed full-pol decomposition powers with Freeman (F3D) and Yamaguchi four-component decomposition with rotation (Y4R) powers over different areas for FP C-band Radarsat-2 SAR data over SF, USA. (a) F3D. (b) Y4R. (c) Proposed. (d) F3D: OU. (e) Y4R: OU. (f) Proposed: OU. (g) F3D: U. (h) Y4R: U. (i) Proposed: U. (j) F3D: O. (k) Y4R: O. (l) Proposed: O.

the value of θ_{FP} can suitably characterize it as even-bounce scattering. Fig. 3 corroborates these observations.

Over the urban area ("U"), the sample mean of the even-bounce scattering power, P_d^{FP}, has increased by 0.3 and 0.15 dB, as compared to F3D and Y4R, respectively. Besides, the diffused scattering powers have decreased over this area. A similar result can also be seen in the ALOS-2 Mumbai image.

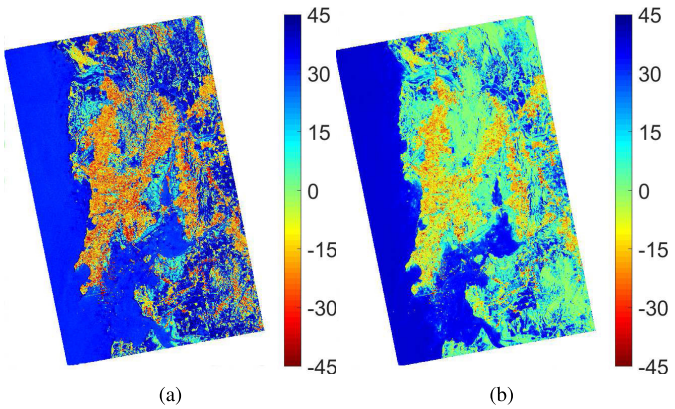

Fig. 9. Images of $\overline{\chi}$ and θ_{CP} for ALOS-2 simulated CP SAR data. (a) $\overline{\chi}$. (b) θ_{CP}.

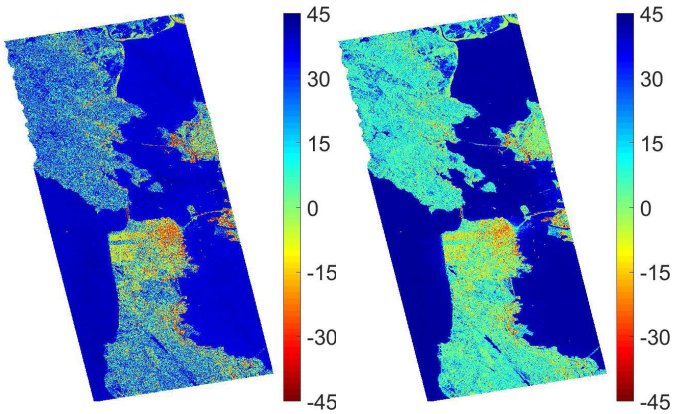

Fig. 10. Images of $\overline{\chi}$ and θ_{CP} for RS-2 simulated CP SAR data. (a) $\overline{\chi}$. (b) θ_{CP}.

Fig. 8 shows the decomposed scattering power images, along with the percentage of the scattering power components over the SF C-band Radarsat-2 image.

The volume scattering component dominates over the rotated urban area ("OU") according to F3D and Y4R: its power is 61.2% for F3D and 51.6% for Y4R. In contrast, the proposed technique correctly shows dominant even-bounce scattering power of 55.5% and a diffused scattering power of 34.2%. However, differences in even-bounce power between "U" and "OU" is due to variations in scattering randomness which can be observed in Fig. 4. Hence, the proposed technique enhances the even-bounce scattering power by approximately 13% and 18% when compared with F3D and Y4R, respectively.

Over the ocean area, an increase of odd-bounce scattering power by ≈4% is apparent from the plots. As discussed earlier, the diffused scattering power over the urban area has decreased by ≈7.3% from F3D and ≈0.7% from Y4R. The odd-bounce scattering power has decreased by ≈2% to 5% from F3D and Y4R, respectively. Besides this, the helix power component (P_h^{FP}) obtained from the Y4R decomposition is negligible for most of the targets as compared to the other three scattering power components. Therefore, the proposed technique ascertains its ability to extract pertinent information about coherent targets and better characterizes roll-invariant targets from FP SAR data.

B. Compact Polarimetry

We simulated hybrid-CP SAR data from the ALOS-2 L-band FP SAR data over Mumbai and from the RS-2 C-band FP SAR data over SF. We obtained the 2×2 covariance matrices $\mathbf{C}_2$ from the 3×3 covariance matrices of FP data as a function of the transmitting ellipticity χ and orientation angle ψ. In this study, we simulated $\mathbf{C}_2$ with the assumption of right circular polarization on transmit, $\chi = -45°$ and $\psi = 0°$ [39]. This particular configuration simulates compact-pol data for a perfect circular polarization on transmit.

We compare the target scattering-type parameter, θ_{CP} with the ellipticity parameter $\overline{\chi}$ over the same areas used for the analysis of the FP images. Similar to θ_{FP}, the values of θ_{CP} and $\overline{\chi}$ vary from $-45°$ to $45°$ and, thus, are comparable.

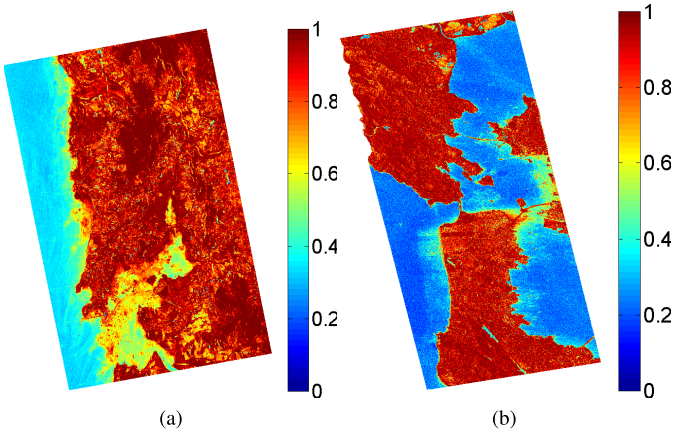

Fig. 11. Images of H for (a) ALOS-2 CP and (b) RS-2 CP SAR data over Mumbai and SF, respectively.

$\theta_{\mathrm{CP}} = -45°$ for pure even-bounce scattering and $\theta_{\mathrm{CP}} = 45°$ for pure odd-bounce scattering, whereas $\theta_{\mathrm{CP}} = 0°$ for diffused scattering.

Figs. 9 and 10 show $\overline{\chi}$ and θ_{CP} over Mumbai and SF, respectively, and the entropy plots are shown in Fig. 11. Both parameters span from odd-bounce scattering to even-bounce scattering characteristics.

1) Comparison of θ_{CP} With $\overline{\chi}$: Fig. 12 shows histograms and notched boxplots of θ_{CP} and $\overline{\chi}$ over the ALOS-2 L-band image. The difference between θ_{CP} and $\overline{\chi}$ is most noticeable in two regions: 1) region "O," in blue, which is over the ocean surface and 2) region "F," in green, which is over a forested area. In region "O," the value of $\overline{\chi}$ varies from ≈30° to 32° whereas, θ_{CP} varies from ≈37° to 39°. Moreover, the value of m_{CP} is high in the region "O," which confirms that the EM wave is majorly polarized in this region.

Over the region "F," the value of m_{CP} varies from ≈0.07 to 0.15, indicating low polarization due to random scattering. Here, θ_{CP} fluctuates around 0.5°, while $\overline{\chi}$ varies from ≈−18° to 12°. Therefore, similar to θ_{FP}, θ_{CP} suitably characterizes distributed targets than $\overline{\chi}$ due to its better consistency.

Fig. 13 shows similar results for the C-band RS-2 CP SAR data: ocean surface ("O") in blue, orthogonal urban ("U") in red, and rotated urban ("RU") in magenta. Over the region

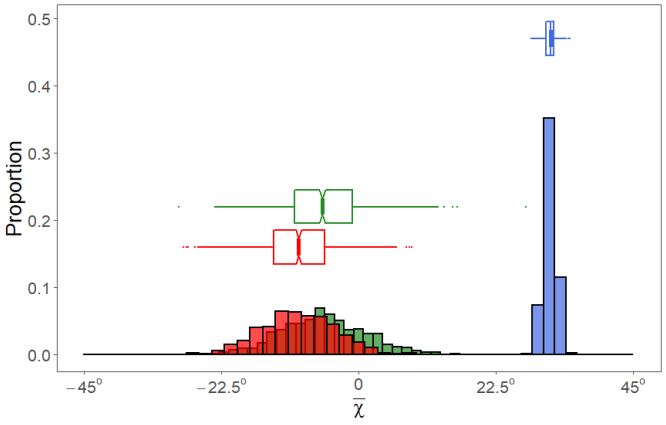

(a) $\overline{\chi}$

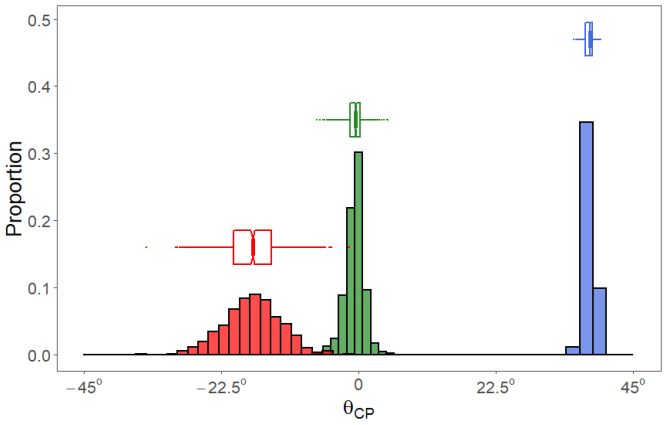

(b) θ_{CP}

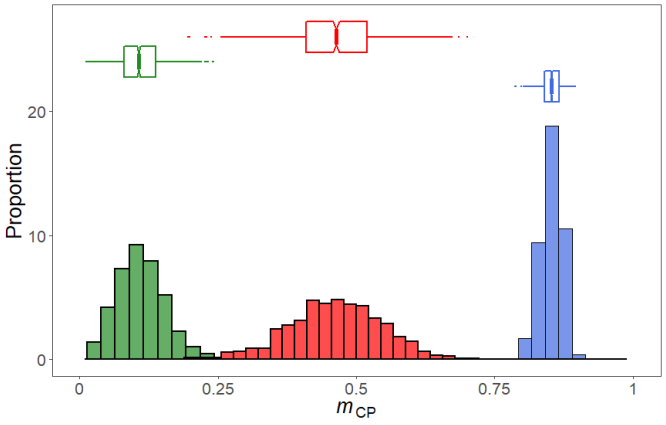

(c) m_{CP}

Fig. 12. Comparison of θ_{CP} with $\overline{\chi}$ and m_{CP} for urban (red), forest (green), and ocean (blue) over CP ALOS-2 L-band data. (a) $\overline{\chi}$. (b) θ_{CP}. (c) m_{CP}.

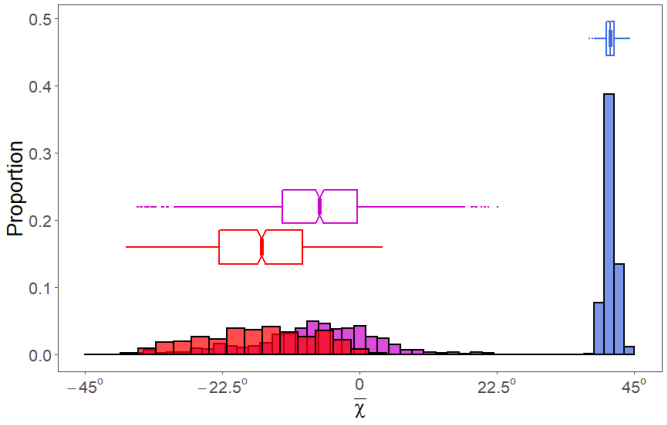

(a)

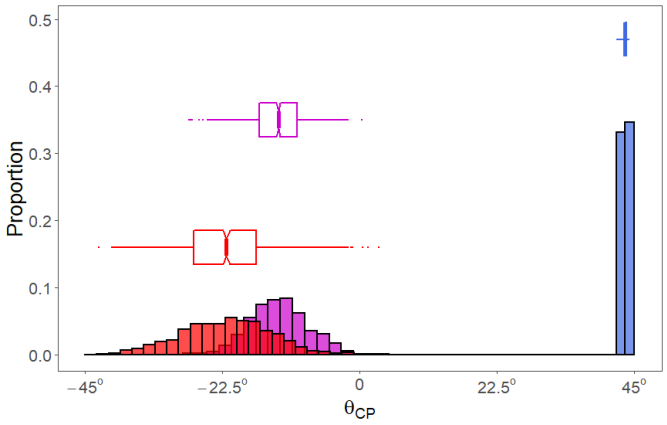

(b)

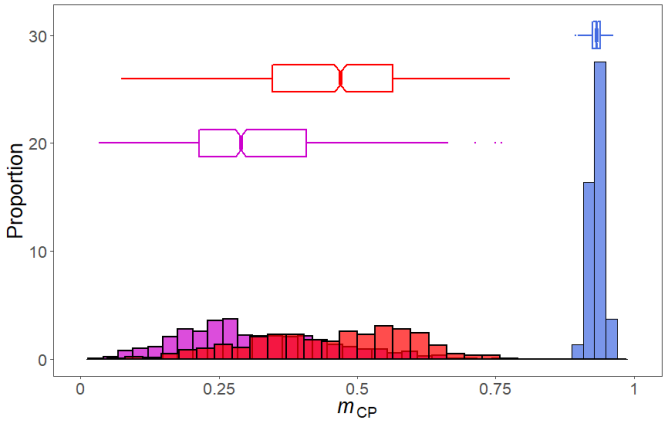

(c)

Fig. 13. Comparison of θ_{CP} with $\overline{\chi}$ and m_{CP} for urban (red), rotated urban (magenta), and ocean (blue) over CP RS-2 C-band data. (a) $\overline{\chi}$. (b) θ_{CP}. (c) m_{CP}.

"O," the value of θ_{CP} is ≈3°–5° higher than $\overline{\chi}$. Therefore, the performance of θ_{CP} is better than $\overline{\chi}$ for the ocean area. Furthermore, θ_{CP} fluctuates around −21° over "U," and −13° over "OU," whereas, the variation of $\overline{\chi}$ is similar over the region "U."

2) Decomposed Power Components: Fig. 14 shows the results of the scattering powers for the L-band ALOS-2 SAR data using the S-Ω, m-χ, and the proposed technique. Overall, we can notice that the results of the proposed technique are better than S-Ω and m-χ decomposition techniques. The P_s^{CP} power is marginally higher than S-Ω and m-χ over the ocean region "O." However, we can notice a decrease of ≈9.5 dB in the P_d^{CP} power by the proposed technique when compared to S-Ω over this region. In contrast, the difference in the even-bounce power between m-χ, and the proposed technique is of 6.13 dB.

The value of P_d^{CP} for both S-Ω and m-χ is ≈7.03 dB over the urban area "U", whereas P_d^{CP} is ≈7.47 dB for

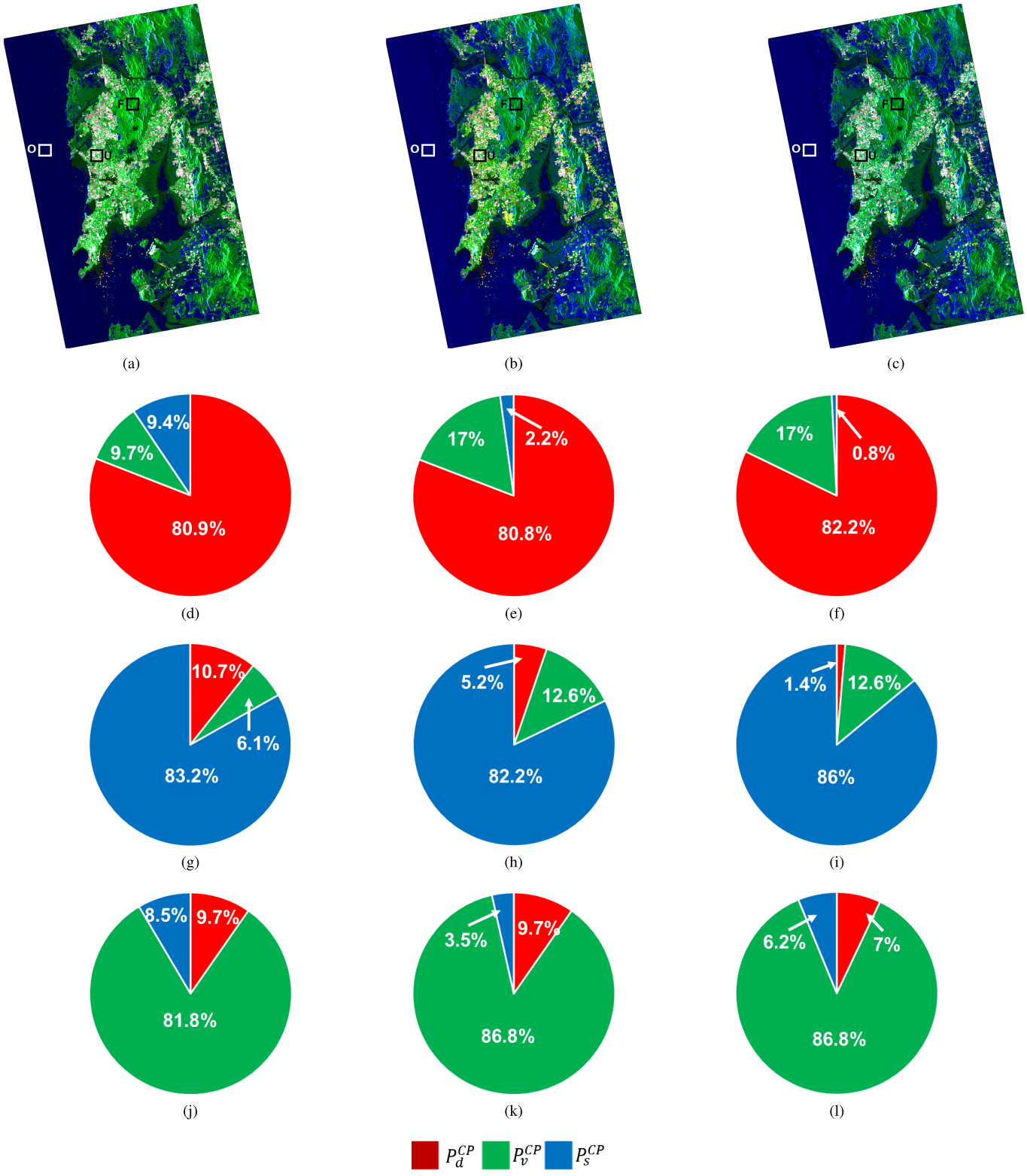

Fig. 14. Comparison of the proposed compact-pol decomposition powers with S-Ω and m-χ decomposition powers over different areas for the simulated CP L-band ALOS-2 SAR data over Mumbai, India. (a) S-Ω. (b) m-χ. (c) Proposed. (d) S-Ω: U. (e) m-χ: U. (f) Proposed: U. (g) S-Ω: O. (h) m-χ: O. (i) Proposed: O. (j) S-Ω: F. (k) m-χ: F. (l) Proposed: F.

the proposed technique. Therefore, the proposed technique discriminates better odd-bounce and even-bounce scattering than S-Ω and m-χ.

P_v^{CP} ≈ -6.54 dB for S-Ω and ≈ -6.35 dB for both m-χ and the proposed technique over the forest area. Moreover, we can notice that the diffused power for both m-χ, and the

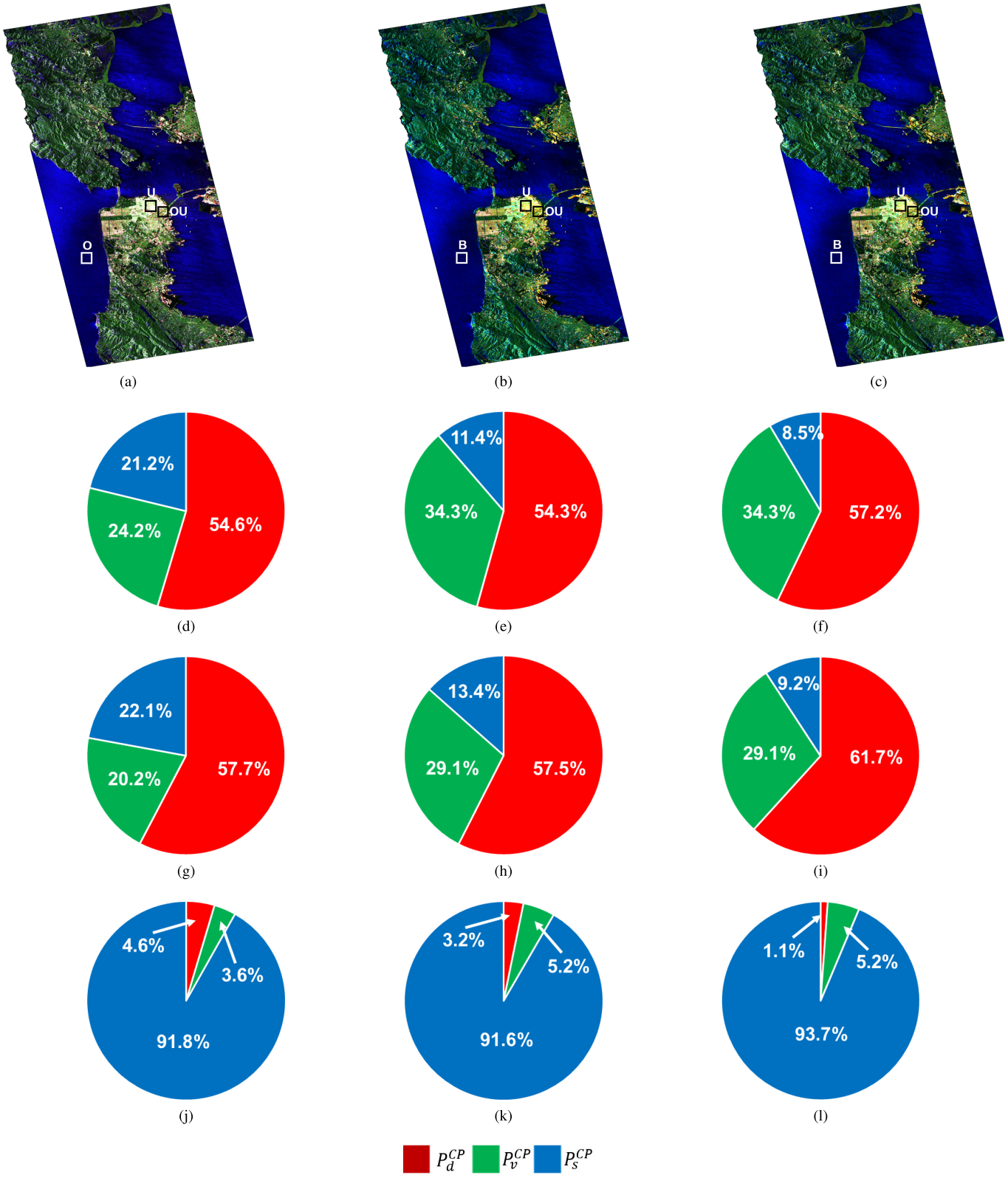

Fig. 15. Comparison of the proposed compact-pol decomposition powers with S-Ω and m-χ decomposition powers over different areas for the simulated CP C-band RS-2 SAR data over SF, USA. (a) S-Ω. (b) m-χ. (c) Proposed. (d) S-Ω: OU. (e) m-χ: OU. (f) Proposed: OU. (g) S-Ω: U. (h) m-χ: U. (i) Proposed: U. (j) S-Ω: O. (k) m-χ: O. (l) Proposed: O.

proposed technique are identical for target areas in the scene. This is because both m-χ and the proposed technique use the depolarization fraction $(1 - m_{\mathrm{CP}})$ of the total power to compute the diffused scattering power component. However, the presence of small, even-bounce and odd-bounce scattering powers in the forest area might be due to specific structural

effects and the ability of the L-band SAR wave to penetrate the forest canopy.

We notice from the scattering power components that the dominant scattering mechanism for each area is comparable with S-Ω, m-χ, and the proposed technique. Essentially, this similarity among different techniques indicates their equivalent ability to identify dominant scatterers in the scene. However, the proposed technique provides marginally better results than the other two over urban and ocean areas for CP SAR data.

In the following, we make quantitative assessments of three-component decomposition powers from S-Ω, m-χ, and the proposed technique using the C-band RS-2 CP data. We used small patches over urban ("U"), ocean ("O"), and rotated urban ("OU") areas for comparison.

The odd-bounce scattering power over the ocean area is better with the proposed technique than S-Ω and m-χ. Besides, the even-bounce power is significantly lower by $\approx$15 dB and $\approx$9 dB for the proposed technique than S-Ω and m-χ, respectively. This aspect suggests that the proposed technique adequately quantifies the dominant scattering mechanism over the ocean surface.

The proposed technique increases the even-bounce scattering power over the rotated urban area. The even-bounce scattering power obtained from the proposed technique is 0.31 dB higher than S-Ω and m-χ. However, both m-χ and the proposed technique detect small P_v^{CP} power of -6.15 dB over this area. The presence of this diffused scattering power is likely due to the cross-polarization component of the EM wave generated by oriented urban areas about the radar line of sight [40], [41]. Hence, the value of H over this region is higher than the urban area by 20%–30% as seen in Fig. 11.

Over the urban area, the even-bounce scattering power P_d^{CP} from the proposed technique is higher than S-Ω and m-χ, while P_d^{CP} for both m-χ and S-Ω are similar. Compared to S-Ω, we notice a 0.36 dB increase in the P_d^{CP} power component for the proposed technique. On the other hand, the P_s^{CP} power is considerably lower ($\approx$2 dB) for the proposed technique than S-Ω and m-χ. This indicates the ability of the proposed technique to quantify better the amount of pure scattering characteristics.

Fig. 15 shows the decomposed power images, along with the percentages of P_d^{CP}, P_v^{CP}, and P_s^{CP} over the rotated urban, ocean, and forest areas. All the dominant power components are similar across all the targets. Over the rotated urban area, the proposed technique retrieves around 3% more the even-bounce scattering power compared to the other methods.

In summary, it should also be noted that S-Ω, m-χ, and the proposed technique jointly use both the 2-D Barakat degree of polarization and the received wave information in terms of the elements of the covariance matrix. This joint utilization of the wave information helps better target characterization while improving the scattering powers.

IV. Conclusion

We proposed two unique roll-invariant scattering-type parameters: θ_{FP}, for FP, and θ_{CP}, for CP, to characterize different targets from SAR data. These two parameters are derived by jointly using both 3-D and 2-D Barakat degree of polarization and received wave information from SAR data.

We have shown that due to the joint utilization of the 3-D and 2-D Barakat degree of polarization and received wave information, θ_{FP} and θ_{CP} can extract more purity in the EM wave as compared to α and χ. Experimental results support that θ_{FP} and θ_{CP} better characterize rotated urban and vegetation areas than α and χ. Moreover, the variability of these proposed parameters over vegetation areas is much lower than α and χ. This aspect indicates a promising consistency of these parameters over distributed targets, similar to even and odd-bounce targets.

The parameters are then utilized to derive nonmodel-based three-component scattering power decomposition techniques for both FP and CP SAR data. It is noteworthy that the formulations of these two techniques are equivalent for both the SAR imaging modes. Traditional model-based decomposition techniques are limited to the optimization of the received covariance matrix while ignoring the utilization of the amount of polarization in the scattered wave. In this perspective, the use of the 3-D and 2-D Barakat degree of polarization has suitably enhanced the ability to discriminate distinct targets within a resolution cell. This feature is also evident from the plots of $\overline{\alpha}/\theta_{\mathrm{FP}}$ for FP data and $\overline{\chi}/\theta_{\mathrm{CP}}$ for CP data. Besides, it can be seen from the study that, the parameters, θ_{FP} and θ_{CP} together with the three scattering power components can adequately characterize complete scattering mechanisms from a target.

Results show that our proposed technique performs better than the Freeman-Durden three-component decomposition (F3D), Yamaguchi 4-component decomposition with rotation (Y4R) for FP data, and also better than S-Ω, m-χ for CP data. Moreover, the proposed decomposition techniques are intuitive and model-free. Hence, the overestimation of any power component is absent, and the polarized power component has improved with the utilization of the Barakat degree of polarization. Furthermore, the proposed technique produces nonnegative power components, which is a significant drawback of several model-based decomposition techniques, as reported in numerous studies. Moreover, the results also show the improvement of decomposed scattering powers over diverse regions.

Specifically, as addressed earlier, coherent power components have increased, which indicates the enhanced ability to extract coherent scatterers from the scene. Notably, the improvement of coherent power estimation is evident in rotated urban areas for FP data due to the roll-invariant nature of the scattering-type parameter, where both F3D and Y4R increases the volume power component.

The proposed technique identifies even-bounce as the dominant scattering power, which is also significantly higher than the volume component. Another essential feature is that the decomposition powers are stable, that is the powers are insensitive to noise, which is vital for an effective decomposition algorithm. Thus this proposed decomposition technique has excellent potential for land use and land cover analysis using both FP and CP SAR data.

APPENDIX

In this section, we prove the roll-invariant nature of θ_{FP} and θ_{CP}, we obtain their ranges analytically, and we justify these properties from a physical perspective. We also show the relationships between θ_{FP} and α, and between θ_{CP} and χ.

A. Range of θ_{FP} and θ_{CP}

1) For θ_{FP}: The expression of θ_{FP} is given as

$$\theta_{\mathrm{FP}} = \tan^{-1}(A) \tag{19}$$

where

$$A = \frac{m_{\mathrm{FP}}\,\mathrm{Span}\,(T_{11} - T_{22} - T_{33})}{T_{11}\,(T_{22} + T_{33}) + m_{\mathrm{FP}}^2\,\mathrm{Span}^2}. \tag{20}$$

The range of A can be obtained by considering three coherency matrices defining the boundary curve of the feasible scattering region [1]

$$\text{Case 1: } \mathbf{T}_{(I)} = \begin{bmatrix} 1 & 0 & 0 \\ 0 & \rho & 0 \\ 0 & 0 & \rho \end{bmatrix}; \quad 0 \le \rho \le 1. \tag{21}$$

The 3-D polarization Barakat degree of polarization, m_{FP} is expressed in terms of the boundary parameter ρ as

$$m_{\mathrm{FP}} = \left(1 - \frac{27\rho^2}{(2\rho+1)^3}\right)^{\frac{1}{2}} \tag{22}$$

and

$$A = \frac{m_{\mathrm{FP}}\left(1 - 4\rho^2\right)}{2\rho + m_{\mathrm{FP}}^2\left(4\rho^2 + 4\rho + 1\right)}. \tag{23}$$

Using (22) and (23) in the range of ρ, we get $0 \le A \le 1$.

For the second case

$$\text{Case 2: } \mathbf{T}_{(II)} = \begin{bmatrix} 2\rho - 1 & 0 & 0 \\ 0 & 1 & 0 \\ 0 & 0 & 1 \end{bmatrix}; \quad 0.5 \le \rho \le 1 \tag{24}$$

with

$$m_{\mathrm{FP}} = \left(1 - \frac{27\,(2\rho - 1)}{(2\rho+1)^3}\right)^{\frac{1}{2}} \tag{25}$$

and

$$A = \frac{m_{\mathrm{FP}}\,(2\rho+1)\,(2\rho-3)}{2\,(2\rho-1) + m_{\mathrm{FP}}^2\,(2\rho+1)^2}. \tag{26}$$

For the third case

$$\text{Case 3: } \mathbf{T}_{(III)} = \begin{bmatrix} 0 & 0 & 0 \\ 0 & 1 & 0 \\ 0 & 0 & 2\rho \end{bmatrix}; \quad 0.5 \le \rho \le 1. \tag{27}$$

Therefore, for, Case 3, $m_{\mathrm{FP}} = 1$ and $A = -1$. Hence, combining the two cases (i.e., Case 2 and Case 3), we get, $-1 \le A \le 0$. This shows that, $-1 \le A \le 1$, and therefore, $-45^\circ \le \theta_{\mathrm{FP}} \le 45^\circ$.

2) For θ_{CP}: In analogy to θ_{FP}, the expression of θ_{CP} is given as

$$\theta_{\mathrm{CP}} = \tan^{-1}(X) \tag{28}$$

where

$$X = \frac{m_{\mathrm{CP}}\,\mathrm{Span}\,(\mathrm{OC} - \mathrm{SC})}{\mathrm{OC} \times \mathrm{SC} + m_{\mathrm{CP}}^2\,\mathrm{Span}^2}. \tag{29}$$

The range of X can be obtained by considering two cases of the covariance matrices

$$\text{Case 1: } \mathbf{C}_{2(I)} = \frac{1}{4}\begin{bmatrix} 2\rho+1 & i(2\rho-1) \\ -i(2\rho-1) & 2\rho+1 \end{bmatrix}; \quad 0 \le \rho \le 0.5. \tag{30}$$

The 2-D Barakat degree of polarization, m_{CP} is expressed in terms of ρ as

$$m_{\mathrm{CP}} = \left(1 - \frac{8\rho}{\left(4\rho^2 + 4\rho + 1\right)}\right)^{\frac{1}{2}} \tag{31}$$

and

$$X = \frac{m_{\mathrm{CP}}\left(1 - 4\rho^2\right)}{2\rho + m_{CP}^2\left(4\rho^2 + 4\rho + 1\right)}. \tag{32}$$

Using (31) and (32) in the range of ρ, we get $0 \le X \le 1$.

For the second case,

$$\text{Case 2: } \mathbf{C}_{2(II)} = \frac{1}{4}\begin{bmatrix} 2\rho+1 & -i(2\rho-1) \\ i(2\rho-1) & 2\rho+1 \end{bmatrix}; \quad 0.5 \le \rho \le 1 \tag{33}$$

with

$$m_{\mathrm{CP}} = \left(1 - \frac{8\rho}{\left(4\rho^2 + 4\rho + 1\right)}\right)^{\frac{1}{2}} \tag{34}$$

and

$$X = \frac{m_{\mathrm{CP}}\left(4\rho^2 - 1\right)}{2\rho + m_{\mathrm{CP}}^2\left(4\rho^2 + 4\rho + 1\right)}. \tag{35}$$

Using (34) and (35) in the range of ρ, we get $-1 \le X \le 0$. Therefore, combining the two ranges of X we get, $-1 \le X \le 1$, and hence, $-45^\circ \le \theta_{\mathrm{CP}} \le 45^\circ$.

B. Roll-Invariant Nature of θ_{FP}

In order to show that θ_{FP} is a roll-invariant parameter, let the coherency matrix $\mathbf{T}$ be unitarily rotated by $\mathbf{R}(\Psi)$ as

$$\mathbf{T}(\Psi) = \mathbf{R}(\Psi)\mathbf{T}\mathbf{R}(\Psi)^{-1} \tag{36}$$

where

$$\mathbf{R}(\Psi) = \begin{bmatrix} 1 & 0 & 0 \\ 0 & \cos 2\Psi & \sin 2\Psi \\ 0 & -\sin 2\Psi & \cos 2\Psi \end{bmatrix}. \tag{37}$$

With this

$$\begin{aligned} T_{11}(\Psi) &= T_{11} \\ T_{22}(\Psi) &= T_{22}\cos^2(2\Psi) + T_{32}\cos(2\Psi)\sin(2\Psi) \\ &\quad + T_{23}\cos(2\Psi)\sin(2\Psi) + T_{33}\sin^2(2\Psi) \\ T_{33}(\Psi) &= T_{22}\sin^2(2\Psi) - T_{32}\cos(2\Psi)\sin(2\Psi) \\ &\quad - T_{23}\cos(2\Psi)\sin(2\Psi) + T_{33}\cos^2(2\Psi). \end{aligned} \tag{38}$$

Therefore, $T_{11}(\Psi) - T_{22}(\Psi) - T_{33}(\Psi) = T_{11} - T_{22} - T_{33}$ and $T_{22}(\Psi) + T_{33}(\Psi) = T_{22} + T_{33}$ i.e., both $T_{11} - T_{22} - T_{33}$ and $T_{22} + T_{33}$ are independent of the unitary rotation by an angle Ψ. The total power (i.e., Span), and the 3-D Barakat degree of polarization m_{FP} are independent of Ψ. Hence, we conclude that the proposed scattering-type parameter for FP SAR

$$\theta_{\text{FP}} = \tan^{-1}\left(\frac{m_{\text{FP}}\,\text{Span}\,(T_{11} - T_{22} - T_{33})}{T_{11}\,(T_{22} + T_{33}) + m_{\text{FP}}^2\,\text{Span}^2}\right) \tag{39}$$

is independent of Ψ, i.e., it is a roll-invariant parameter.

C. Roll-Invariant Nature of θ_{CP}

The 2×2 covariance matrix can be expressed in terms of the elements of the Stokes vector $\vec{\mathbf{S}} = [S_0, S_1, S_2, S_3]$ as

$$\mathbf{C}_2 = \frac{1}{2}\begin{bmatrix} S_0 + S_1 & S_2 + iS_3 \\ S_2 - iS_3 & S_0 - S_1 \end{bmatrix}. \tag{40}$$

Let the $\mathbf{C}_2$ matrix be unitarily rotated by $\mathbf{R}(\Psi)$ as $\mathbf{C}_2(\Psi) = \mathbf{R}(\Psi)\mathbf{C}_2\mathbf{R}(\Psi)^{-1}$, where the rotation matrix is

$$\mathbf{R}(\Psi) = \begin{bmatrix} \cos(\Psi) & -\sin(\Psi) \\ \sin(\Psi) & \cos(\Psi) \end{bmatrix}. \tag{41}$$

The elements of the $\mathbf{C}_2(\Psi)$ matrix are

$$\begin{aligned}
c_{11}(\Psi) &= \cos^2\Psi(S_0 + S_1) - \cos\Psi\sin\Psi(S_2 - iS_3) \\
&\quad - \cos\Psi\sin\Psi(S_2 + iS_3) + \sin^2\Psi(S_0 - S_1) \\
c_{12}(\Psi) &= \cos\Psi\sin\Psi(S_0 + S_1) - \sin^2\Psi(S_2 - iS_3) \\
&\quad + \cos^2\Psi(S_2 + iS_3) - \cos\Psi\sin\Psi(S_0 - S_1) \\
c_{21}(\Psi) &= \cos\Psi\sin\Psi(S_0 + S_1) + \cos^2\Psi(S_2 - iS_3) \\
&\quad - \sin^2\Psi(S_2 + iS_3) - \cos\Psi\sin\Psi(S_0 - S_1) \\
c_{22}(\Psi) &= \sin^2\Psi(S_0 + S_1) - \cos\Psi\sin\Psi(S_2 - iS_3) \\
&\quad - \cos\Psi\sin\Psi(S_2 + iS_3) + \cos^2\Psi(S_0 - S_1).
\end{aligned}$$

The total power $S_0 = c_{11}(\Psi) + c_{22}(\Psi)$ and the fourth element of the Stokes vector $S_3 = -i(c_{12}(\Psi) - c_{21}(\Psi))$ are independent of the rotation angle Ψ. Since S_0 and S_3 are independent of Ψ, then $\text{SC} = (S_0 - S_3)/2$ and $\text{OC} = (S_0 + S_3)/2$ are also independent of Ψ, i.e., both parameters are roll-invariant.

Alongside, note that $|\mathbf{C}_2|$ and $\text{Tr}(\mathbf{C}_2)$ are roll-invariant, where $|\cdot|$ is the determinant and $\text{Tr}(\cdot)$ is the trace of the matrix. Therefore, the 2-D Barakat degree of polarization, $m_{\text{CP}} = (1 - (4|\mathbf{C}_2|)/((\text{Tr}(\mathbf{C}_2))^2))^{1/2}$ is also roll-invariant. Hence, we conclude that the proposed scattering-type parameter for CP SAR

$$\theta_{\text{CP}} = \tan^{-1}\left(\frac{m_{\text{CP}}\,S_0\,(\text{OC} - \text{SC})}{\text{OC} \times \text{SC} + m_{\text{CP}}^2\,S_0^2}\right) \tag{42}$$

is independent of Ψ, i.e., it is a roll-invariant parameter.

D. Relationships of θ_{FP} With α, and of θ_{CP} With χ

1) θ_{FP} With α: Note that

$$\frac{T_{11}}{\text{Span}} = \sum_{i=1}^{3} p_i \cos^2\alpha_i \tag{43}$$

where $(\alpha_i)_{i=1,2,3}$ are the individual scattering-type parameters obtained from the α-β parametrization of the Cloude-Pottier target scattering vector.

Let

$$\tan\eta_1 = \frac{T_{11}}{m_{\text{FP}}\,\text{Span}} = \frac{\sum_{i=1}^{3} p_i \cos^2\alpha_i}{\sqrt{1 - \prod_{i=1}^{3} 3p_i}} \tag{44}$$

and

$$\tan\eta_2 = \frac{T_{22} + T_{33}}{m_{\text{FP}}\,\text{Span}} = \frac{1 - \sum_{i=1}^{3} p_i \cos^2\alpha_i}{\sqrt{1 - \prod_{i=1}^{3} 3p_i}}. \tag{45}$$

Then

$$\begin{aligned}
\tan(\eta_1 - \eta_2) &= \frac{\frac{\sum_{i=1}^{3} p_i\cos^2\alpha_i}{\sqrt{1-\prod_{i=1}^{3}3p_i}} - \frac{1-\sum_{i=1}^{3} p_i\cos^2\alpha_i}{\sqrt{1-\prod_{i=1}^{3}3p_i}}}{1 + \frac{\sum_{i=1}^{3} p_i\cos^2\alpha_i}{\sqrt{1-\prod_{i=1}^{3}3p_i}}\frac{1-\sum_{i=1}^{3} p_i\cos^2\alpha_i}{\sqrt{1-\prod_{i=1}^{3}3p_i}}} \\
&= \frac{\frac{2\sum_{i=1}^{3} p_i\cos^2\alpha_i - 1}{\sqrt{1-\prod_{i=1}^{3}3p_i}}}{1 + \frac{\left(\sum_{i=1}^{3} p_i\cos^2\alpha_i\right)\left(1-\sum_{i=1}^{3} p_i\cos^2\alpha_i\right)}{1-\prod_{i=1}^{3}3p_i}}.
\end{aligned} \tag{46}$$

Hence, the expression of θ_{FP} is given in terms of $(p_i)_{i=1,2,3}$ and $(\alpha_i)_{i=1,2,3}$ as

$$\begin{aligned}
\tan\theta_{\text{FP}} &= \frac{\text{Num}}{\text{Den}}, \text{ in which} \\
\text{Num} &= \left(2\sum_{i=1}^{3} p_i\cos^2\alpha_i - 1\right)\sqrt{1 - \prod_{i=1}^{3} 3p_i}, \text{ and} \\
\text{Den} &= 1 - \prod_{i=1}^{3} 3p_i \\
&\quad + \left(\sum_{i=1}^{3} p_i\cos^2\alpha_i\right)\left(1 - \sum_{i=1}^{3} p_i\cos^2\alpha_i\right).
\end{aligned} \tag{47}$$

Therefore, it can be noticed that θ_{FP} is a function of $\sum_{i=1}^{3} p_i\cos^2\alpha_i$, and the 3-D Barakat degree of polarization, $(1 - \prod_{i=1}^{3} 3p_i)^{1/2}$. Similarly, in [42], $N_{11} = \sum_{i=1}^{3} p_i\cos^2\alpha_i$ is defined as the surface scattering fraction and is interpreted as the fraction of odd-bounce scattering from total backscattered power. Furthermore, it can also be related to the fraction of right-left circularly polarized response from total backscattered power measured in a circular basis.

2) θ_{CP} With χ: The ellipticity χ is defined in terms of the elements of Stokes vector, $\vec{\mathbf{S}} = [S_0, S_1, S_2, S_3]$ as

$$\sin 2\chi = -\frac{S_3}{m_{\text{CP}}\,S_0} \tag{48}$$

where m_{CP} is the 2-D Barakat degree of polarization, and

$$\text{OC} = \frac{S_0 + S_3}{2} \quad \text{and} \quad \text{SC} = \frac{S_0 - S_3}{2}. \tag{49}$$

Therefore, θ_{CP} is given in terms of χ and m_{CP} as

$$\begin{aligned}\tan\theta_{\mathrm{CP}} &= \frac{m_{\mathrm{CP}}\,\mathrm{Span}\,(\mathrm{OC}-\mathrm{SC})}{\mathrm{OC}\times\mathrm{SC}+m_{\mathrm{CP}}^2\,\mathrm{Span}^2}\\ &= \frac{m_{\mathrm{CP}}S_0S_3}{\frac{S_0^2-S_3^2}{4}+m_{\mathrm{CP}}^2S_0^2} = \frac{4m_{\mathrm{CP}}S_0S_3}{S_0^2-S_3^2+4m_{\mathrm{CP}}^2S_0^2}\\ &= \frac{4m_{\mathrm{CP}}\,(S_3/S_0)}{1-(S_3/S_0)^2+4m_{\mathrm{CP}}^2} = \frac{4m_{\mathrm{CP}}\,(-m_{\mathrm{CP}}\sin 2\chi)}{1-m_{\mathrm{CP}}^2\sin^2 2\chi+4m_{\mathrm{CP}}^2}\\ &= -\frac{4m_{\mathrm{CP}}^2\sin 2\chi}{1-m_{\mathrm{CP}}^2\sin^2 2\chi+4m_{\mathrm{CP}}^2}.\end{aligned}$$

ACKNOWLEDGMENT

The authors would like to thank Dr. Eric Pottier, Prof. José J. Gil, and Prof. Christian Brosseau for their valuable inputs to enrich the scientific content of this manuscript. They would like to thank MAXAR Technologies Ltd., formerly MacDonald, Dettwiler, and Associates (MDA), for providing RADARSAT-2 data and JAXA for providing the ALOS-2 PALSAR data. They also acknowledge the GEO-AWS Earth Observation Cloud Credits Program through the project—AWS4AgriSAR-Crop inventory mapping from SAR data on cloud computing platform. Debanshu Ratha (coauthor) would like to thank the Council of Scientific and Industrial Research (CSIR) for supporting his doctoral studies.

REFERENCES

[1] S. R. Cloude and E. Pottier, "An entropy based classification scheme for land applications of polarimetric SAR," *IEEE Trans. Geosci. Remote Sens.*, vol. 35, no. 1, pp. 68–78, Jan. 1997.

[2] R. Touzi, "Target scattering decomposition in terms of roll-invariant target parameters," *IEEE Trans. Geosci. Remote Sens.*, vol. 45, no. 1, pp. 73–84, Jan. 2007.

[3] D. Ratha, E. Pottier, A. Bhattacharya, and A. C. Frery, "A PolSAR scattering power factorization framework and novel roll-invariant parameter-based unsupervised classification scheme using a geodesic distance," *IEEE Trans. Geosci. Remote Sens.*, vol. 58, no. 5, pp. 3509–3525, May 2019.

[4] A. Freeman and S. L. Durden, "A three-component scattering model for polarimetric SAR data," *IEEE Trans. Geosci. Remote Sens.*, vol. 36, no. 3, pp. 963–973, May 1998.

[5] J.-S. Lee, M. R. Grunes, T. L. Ainsworth, L.-J. Du, D. L. Schuler, and S. R. Cloude, "Unsupervised classification using polarimetric decomposition and the complex wishart classifier," *IEEE Trans. Geosci. Remote Sens.*, vol. 37, no. 5, pp. 2249–2258, Sep. 1999.

[6] J.-S. Lee, M. R. Grunes, E. Pottier, and L. Ferro-Famil, "Unsupervised terrain classification preserving polarimetric scattering characteristics," *IEEE Trans. Geosci. Remote Sens.*, vol. 42, no. 4, pp. 722–731, Apr. 2004.

[7] Y. Yamaguchi, T. Moriyama, M. Ishido, and H. Yamada, "Four-component scattering model for polarimetric SAR image decomposition," *IEEE Trans. Geosci. Remote Sens.*, vol. 43, no. 8, pp. 1699–1706, Aug. 2005.

[8] M. Arii, J. J. van Zyl, and Y. Kim, "A general characterization for polarimetric scattering from vegetation canopies," *IEEE Trans. Geosci. Remote Sens.*, vol. 48, no. 9, pp. 3349–3357, Sep. 2010.

[9] M. Neumann, L. Ferro-Famil, and A. Reigber, "Estimation of forest structure, ground, and canopy layer characteristics from multibaseline polarimetric interferometric SAR data," *IEEE Trans. Geosci. Remote Sens.*, vol. 48, no. 3, pp. 1086–1104, Mar. 2010.

[10] J. J. van Zyl, M. Arii, and Y. Kim, "Model-based decomposition of polarimetric SAR covariance matrices constrained for nonnegative eigenvalues," *IEEE Trans. Geosci. Remote Sens.*, vol. 49, no. 9, pp. 3452–3459, Sep. 2011.

[11] Y. Cui, Y. Yamaguchi, J. Yang, H. Kobayashi, S.-E. Park, and G. Singh, "On complete model-based decomposition of polarimetric SAR coherency matrix data," *IEEE Trans. Geosci. Remote Sens.*, vol. 52, no. 4, pp. 1991–2001, Apr. 2014.

[12] W. An, Y. Cui, and J. Yang, "Three-component model-based decomposition for polarimetric SAR data," *IEEE Trans. Geosci. Remote Sens.*, vol. 48, no. 6, pp. 2732–2739, Jun. 2010.

[13] J.-S. Lee and T. L. Ainsworth, "The effect of orientation angle compensation on coherency matrix and polarimetric target decompositions," *IEEE Trans. Geosci. Remote Sens.*, vol. 49, no. 1, pp. 53–64, Jan. 2011.

[14] Y. Yamaguchi, A. Sato, W.-M. Boerner, R. Sato, and H. Yamada, "Four-component scattering power decomposition with rotation of coherency matrix," *IEEE Trans. Geosci. Remote Sens.*, vol. 49, no. 6, pp. 2251–2258, Jun. 2011.

[15] G. Singh, Y. Yamaguchi, and S.-E. Park, "General four-component scattering power decomposition with unitary transformation of coherency matrix," *IEEE Trans. Geosci. Remote Sens.*, vol. 51, no. 5, pp. 3014–3022, May 2013.

[16] A. Bhattacharya, G. Singh, S. Manickam, and Y. Yamaguchi, "An adaptive general four-component scattering power decomposition with unitary transformation of coherency matrix (AG4U)," *IEEE Geosci. Remote Sens. Lett.*, vol. 12, no. 10, pp. 2110–2114, Oct. 2015.

[17] S.-W. Chen, X.-S. Wang, S.-P. Xiao, and M. Sato, "General polarimetric model-based decomposition for coherency matrix," *IEEE Trans. Geosci. Remote Sens.*, vol. 52, no. 3, pp. 1843–1855, Mar. 2014.

[18] A. Bhattacharya, A. Muhuri, S. De, S. Manickam, and A. C. Frery, "Modifying the Yamaguchi four-component decomposition scattering powers using a stochastic distance," *IEEE J. Sel. Topics Appl. Earth Observ. Remote Sens.*, vol. 8, no. 7, pp. 3497–3506, Jul. 2015.

[19] T. Eltoft and A. P. Doulgeris, "Model-based polarimetric decomposition with higher order statistics," *IEEE Geosci. Remote Sens. Lett.*, vol. 16, no. 6, pp. 992–996, Jun. 2019.

[20] W. An and M. Lin, "A reflection symmetry approximation of multilook polarimetric SAR data and its application to Freeman–Durden decomposition," *IEEE Trans. Geosci. Remote Sens.*, vol. 57, no. 6, pp. 3649–3660, Jun. 2019.

[21] Z. Jiao, J. Yang, C. Yeh, and J. Song, "Modified three-component decomposition method for polarimetric SAR data," *IEEE Geosci. Remote Sens. Lett.*, vol. 11, no. 1, pp. 200–204, Jan. 2014.

[22] Z. Shuang, Y. Xiangchuan, and W. Lu, "Modified version of three-component model-based decomposition for polarimetric SAR data," *J. Syst. Eng. Electron.*, vol. 30, no. 2, pp. 270–277, 2019.

[23] S.-W. Chen, Y.-Z. Li, X.-S. Wang, S.-P. Xiao, and M. Sato, "Modeling and interpretation of scattering mechanisms in polarimetric synthetic aperture radar: Advances and perspectives," *IEEE Signal Process. Mag.*, vol. 31, no. 4, pp. 79–89, Jul. 2014.

[24] J.-C. Souyris, P. Imbo, R. Fjortoft, S. Mingot, and J.-S. Lee, "Compact polarimetry based on symmetry properties of geophysical media: The $\pi/4$ mode," *IEEE Trans. Geosci. Remote Sens.*, vol. 43, no. 3, pp. 634–646, Mar. 2005.

[25] N. Stacy and M. Preiss, "Compact polarimetric analysis of X-band SAR data," in *Proc. EUSAR*, 2006, p. 4.

[26] R. K. Raney, "Hybrid-polarity SAR architecture," *IEEE Trans. Geosci. Remote Sens.*, vol. 45, no. 11, pp. 3397–3404, Nov. 2007.

[27] G. G. Stokes, "On the composition and resolution of streams of polarized light from different sources," *Trans. Cambridge Phil. Soc.*, vol. 9, p. 399, Jan. 1851.

[28] R. K. Raney, J. T. S. Cahill, G. W. Patterson, and D. B. J. Bussey, "The m-chi decomposition of hybrid dual-polarimetric radar data with application to lunar craters," *J. Geophys. Res. Planets*, vol. 117, no. E12, pp. 1991–2012, Dec. 2012, doi: 10.1029/2011JE003986.

[29] A. Bhattacharya, S. De, A. Muhuri, M. Surendar, G. Venkataraman, and A. K. Das, "A new compact polarimetric SAR decomposition technique," *Remote Sens. Lett.*, vol. 6, no. 12, pp. 914–923, Dec. 2015.

[30] S. R. Cloude and E. Pottier, "A review of target decomposition theorems in radar polarimetry," *IEEE Trans. Geosci. Remote Sens.*, vol. 34, no. 2, pp. 498–518, Mar. 1996.

[31] A. Swartz, H. Yueh, J. Kong, L. Novak, and R. Shin, "Optimal polarizations for achieving maximum contrast in radar images," *J. Geophys. Res. Solid Earth*, vol. 93, no. B12, pp. 15252–15260, 1988.

[32] R. Barakat, "Degree of polarization and the principal idempotents of the coherency matrix," *Opt. Commun.*, vol. 23, no. 2, pp. 147–150, Nov. 1977.

[33] R. Barakat, "N-fold polarization measures and associated thermodynamic entropy of n partially coherent pencils of radiation," *Optica Acta Int. J. Opt.*, vol. 30, no. 8, pp. 1171–1182, Aug. 1983.

[34] P. Réfrégier, F. Goudail, P. Chavel, and A. Friberg, "Entropy of partially polarized light and application to statistical processing techniques," *J. Opt. Soc. Amer. A, Opt. Image Sci.*, vol. 21, no. 11, pp. 2124–2134, 2004.

[35] D. J. McLaughlin, N. Allan, E. M. Twarog, and D. B. Trizna, "High resolution polarimetric radar scattering measurements of low grazing angle sea clutter," *IEEE J. Ocean. Eng.*, vol. 20, no. 3, pp. 166–178, Jul. 1995.
[36] I. Brown, S. Mwansasu, and L.-O. Westerberg, "L-band polarimetric target decomposition of mangroves of the Rufiji Delta, Tanzania," *Remote Sens.*, vol. 8, no. 2, p. 140, Feb. 2016.
[37] S.-H. Hong and S. Wdowinski, "Double-bounce component in cross-polarimetric SAR from a new scattering target decomposition," *IEEE Trans. Geosci. Remote Sens.*, vol. 52, no. 6, pp. 3039–3051, Jun. 2014.
[38] T. L. Ainsworth, D. L. Schuler, and J.-S. Lee, "Polarimetric SAR characterization of man-made structures in urban areas using normalized circular-pol correlation coefficients," *Remote Sens. Environ.*, vol. 112, no. 6, pp. 2876–2885, Jun. 2008.
[39] R. Sabry and P. W. Vachon, "A unified framework for general compact and quad polarimetric SAR data and imagery analysis," *IEEE Trans. Geosci. Remote Sens.*, vol. 52, no. 1, pp. 582–602, Jan. 2014.
[40] R. Guinvarc'h and L. Thirion-Lefevre, "Cross-polarization amplitudes of obliquely orientated buildings with application to urban areas," *IEEE Geosci. Remote Sens. Lett.*, vol. 14, no. 11, pp. 1913–1917, Nov. 2017.
[41] D. K. Atwood and L. Thirion-Lefevre, "Polarimetric phase and implications for urban classification," *IEEE Trans. Geosci. Remote Sens.*, vol. 56, no. 3, pp. 1278–1289, Mar. 2018.
[42] J. Praks, E. C. Koeniguer, and M. T. Hallikainen, "Alternatives to target entropy and alpha angle in SAR polarimetry," *IEEE Trans. Geosci. Remote Sens.*, vol. 47, no. 7, pp. 2262–2274, Jul. 2009.

Subhadip Dey (Graduate Student Member, IEEE) received the B.Tech. degree in agricultural engineering from Bidhan Chandra Krishi Viswavidyalaya, Haringhata, India, in 2016, and the M.Tech. degree in aquacultural engineering from the Department of Agricultural and Food Engineering, IIT Kharagpur, Kharagpur, India, in 2018. He is pursuing the Ph.D. degree with Microwave Remote Sensing Laboratory, Centre of Studies in Resources Engineering (CSRE), IIT Bombay, Mumbai, India.

His research interests are land cover classification and agricultural crop mapping and monitoring using synthetic aperture radar data.

Avik Bhattacharya (Senior Member, IEEE) received the integrated M.Sc. degree in mathematics from IIT Kharagpur, Kharagpur, India, in 2000, and the Ph.D. degree in remote sensing image processing and analysis from Télécom ParisTech, Paris, France, and Ariana Research Group, Institut National de Recherche en Informatique et en Automatique (INRIA) Sophia Antipolis, Nice, France, in 2007.

He was a Canadian Government Research Fellow with the Canadian Centre for Remote Sensing (CCRS), Ottawa, ON, Canada. He is an Associate Professor with the Centre of Studies in Resources Engineering (CSRE), IIT Bombay (IITB), Mumbai, India. He is leading the Microwave Remote Sensing Laboratory, CSRE, IITB. His research interests include synthetic aperture radar (SAR) polarimetry, statistical analysis of polarimetric SAR images, and applications of radar remote sensing in agriculture, cryosphere, urban, and planetary studies.

Dr. Bhattacharya is the Founding Chairperson of the IEEE Geoscience and Remote Sensing Society (GRSS) Chapter, Bombay Section. He received the Natural Sciences and Engineering Research Council of Canada Visiting Scientist Fellowship at Canadian Nuclear Laboratories, from 2008 to 2011. He was an Associate Editor of the IEEE GEOSCIENCE AND REMOTE SENSING LETTERS (GRSL). He was a Guest Editor of the IEEE JOURNAL OF SELECTED TOPICS IN APPLIED EARTH OBSERVATIONS AND REMOTE SENSING (J-STARS)—Special Issue on Applied Earth Observations and Remote Sensing, India, in 2017. He was one of the guest editors of the Special Stream on Advanced Statistical Techniques in SAR Image Processing and Analysis at the IEEE GEOSCIENCE AND REMOTE SENSING LETTERS in 2018. He is also the Editor-in-Chief of the IEEE GRSL.

Debanshu Ratha (Member, IEEE) received the five-year integrated M.Sc. degree in mathematics from NISER, Bhubaneswar, India, in 2013. He is pursuing the Ph.D. degree, as a CSIR fellowship awardee, with the Centre of Studies in Resources Engineering (CSRE), IIT Bombay, Mumbai, India.

Since 2013, he has worked in full-time research positions at the Delft Institute of Applied Mathematics, Delft University of Technology (TU Delft), Delft, The Netherlands, and CSRE, IIT Bombay. He has been a Visiting Researcher with the IETR Laboratory, University of Rennes 1, Rennes, France, under the Raman Charpak Fellowship Programme. His research interests include theory of remote sensing and its applications, radar polarimetry, variational analysis, information geometry, graph theory, machine learning, and data fusion.

Mr. Ratha was a recipient of many prestigious scholarships and visiting fellowships in the past.

Dipankar Mandal (Graduate Student Member, IEEE) received the B.Tech. degree in agricultural engineering from Bidhan Chandra Krishi Viswavidyalaya, Haringhata, India, in 2015. He is pursuing the dual M.Tech and Ph.D. degrees in geoinformatics and natural resources engineering with the Centre of Studies in Resources Engineering, IIT Bombay, Mumbai, India.

He was a Visiting Researcher with the Agriculture and Agri-Food Canada (AAFC), Ottawa, ON, Canada, and Carleton University, Ottawa, from October 2018 to February 2019. As a Visiting Researcher, he contributed to synthetic aperture radar (SAR) Intercomparison experiment for crop biophysical parameter estimation within the Joint Experiment for Crop Assessment and Monitoring (JECAM) network of GEO Global Agricultural Monitoring. His research interests include applications of SAR polarimetry for crop classification, vegetation biophysical parameter estimation, deriving vegetation indices, and yield forecasting.

Mr. Mandal was a recipient of the Shastri Research Student Fellowship 2018–2019 Award by the Shastri Indo-Canadian Institute, India.

Alejandro C. Frery (Senior Member, IEEE) received the B.Sc. degree in electronic and electrical engineering from the Universidad de Mendoza, Mendoza, Argentina, in 1985, the M.Sc. degree in applied mathematics (statistics) from the Instituto de Matemática Pura e Aplicada (IMPA), Rio de Janeiro, Brazil, in 1990, and the Ph.D. degree in applied computing from the Instituto Nacional de Pesquisas Espaciais (INPE), São José dos Campos, Brazil, in 1993.

He is the Leader of the Laboratório de Computação Científica e Análise Numérica (LaCCAN), Universidade Federal de Alagoas, Maceió, Brazil. He holds a Huashan Scholar position with the Key Laboratory of Intelligent Perception and Image Understanding of the Ministry of Education, Xidian University, Xi'an, China, for the term 2019–2021. His research interests are statistical computing and stochastic modeling.